



## 2D/2D Z-scheme-based $\alpha$ -Fe<sub>2</sub>O<sub>3</sub> @NGr heterojunction implanted with Pt single-atoms for remarkable photocatalytic hydrogen evolution

Vandung Dao <sup>a,1</sup>, Luis A. Cipriano <sup>b,1</sup>, Sang-Woo Ki <sup>c</sup>, Sunny Yadav <sup>a</sup>, Wenmeng Wang <sup>a</sup>, Giovanni Di Liberto <sup>b</sup>, Kai Chen <sup>a</sup>, Hoki Son <sup>a</sup>, Jin-Kyu Yang <sup>c,\*</sup>, Gianfranco Pacchioni <sup>b,\*</sup>, In-Hwan Lee <sup>a,\*</sup>

<sup>a</sup> Department of Materials Science and Engineering, Korea University, Seoul 02841, Republic of Korea

<sup>b</sup> Dipartimento di Scienza dei Materiali, Università degli Studi di Milano-Bicocca, Via Roberto Cozzi 55, Milano 20125, Italy

<sup>c</sup> Department of Optical Engineering, Kongju National University, Cheonan 31080, Republic of Korea



### ARTICLE INFO

#### Keywords:

Direct Z-scheme  
2D/2D core-shell  
Hematite  
Nitrogen-doped graphene  
Single-atoms  
Photocatalytic hydrogen evolution

### ABSTRACT

Direct Z-scheme designs perform well in light-to-fuel conversion. Here, an active and stable ternary Z-scheme core-shell heterojunction for photocatalytic hydrogen evolution (PHE) is fabricated consisting of hexagonal 2D  $\alpha$ -Fe<sub>2</sub>O<sub>3</sub> (as photocatalyst II) and 2D nitrogen-doped graphene (NGr as photocatalyst I) functionalized with the Pt single-atoms (SAs) cocatalyst. Under visible light, the 2D/2D  $\alpha$ -Fe<sub>2</sub>O<sub>3</sub> @NGr<sub>3</sub>–Pt<sub>SAs</sub> (NGr shell thickness of 3 nm and Pt loading of 0.5 wt%) achieves a remarkable PHE of 6.4  $\mu\text{mol mg}_{\text{cat}}^{-1} \text{ h}^{-1}$ , which is 16.4- and 3.28-times higher than those of free NGr (0.39  $\mu\text{mol mg}_{\text{cat}}^{-1} \text{ h}^{-1}$ ) and binary  $\alpha$ -Fe<sub>2</sub>O<sub>3</sub> @NGr<sub>3</sub> (1.95  $\mu\text{mol mg}_{\text{cat}}^{-1} \text{ h}^{-1}$ ), thus outperforming the currently-advanced PHE catalysts. The outstanding performance is due to the superiority of a direct 2D/2D Z-scheme core-shell fabrication, including a large surface area for light harvesting, facile charge separation and transfer, and the workability of Pt SAs sites. Theoretical investigations provide additional insight into the mechanistic process of the ternary system for PHE reactions.

### 1. Introduction

Hydrogen (H<sub>2</sub>), with the highest gravimetric energy density of all fuel sources, has enormous potential to overcome exigent sustainability and global warming issues [1,2]. Hydrogen is a storable and environmentally friendly fuel with zero carbon emission [3]. Photocatalysis has recently emerged as a promising approach for light-to-hydrogen (LTH) conversion due to its cost-effectiveness, simplicity, and efficiency [4]. Under this process, the electron-hole pairs are readily light-produced on the surface of a relative semiconductor to drive the photocatalytic hydrogen evolution (PHE) [5]. In principle, photocatalysts used for overall water splitting must have a minimum bandgap of 1.23 eV, with the conduction band minimum (CBM) edge located at 0 V (vs. NHE) and the valence band maximum (VBM) at 1.23 V (vs. NHE). In practice, however, the overall water splitting requires an actual bandgap exceeding 1.7 eV due to the thermal losses.

In addition, a direct Z-scheme system with two contacted photocatalysts has been widely utilized for LTH conversion [6]. In this

process, the weaker oxidizing holes produced by light in the first photocatalyst (PC I) prefer to pair with the weaker reducing electrons in the second photocatalyst (PC II) [7]. Combining the electrons and holes in the two photocatalysts increases the redox potential for catalytic processes [8]. The more robust electrons collect on the PC I entity for the reduction reactions, while the PC II functions as a hole-rich entity for the oxidation reactions. Resultantly, a direct Z-scheme platform may outperform its competitors in photocatalytic performance [9]. A promising Z-scheme design for hydrogen evolution is to combine two two-dimensional (2D) materials to create core-shell nanostructures. Such 2D/2D core-shell designs offer unique photocatalysis capabilities. The 2D entities can expose many catalytic reaction sites because of their large surface areas. The 2D/2D core-shell platforms promote light-induced electron and hole separation by increasing the interfacial contact and charge transferability between its constituents [10]. Thus, 2D/2D Z-scheme core-shell constructions meet the requirements of band alignment and effective charge separation and transfer and offer durable photocatalyst systems for PHE applications [11].

\* Corresponding authors.

E-mail addresses: [jkyang.lab@gmail.com](mailto:jkyang.lab@gmail.com) (J.-K. Yang), [gianfranco.pacchioni@unimib.it](mailto:gianfranco.pacchioni@unimib.it) (G. Pacchioni), [ihlee@korea.ac.kr](mailto:ihlee@korea.ac.kr) (I.-H. Lee).

<sup>1</sup> These authors have contributed equally to this work and should be considered co-first authors.

Hematite ( $\alpha\text{-Fe}_2\text{O}_3$ ) has been considered a low-cost and environmentally friendly catalyst for various advanced catalytic processes [12]. With a bandgap of 2.1–2.3 eV [13],  $\alpha\text{-Fe}_2\text{O}_3$  can function as a visible-light-driven photocatalyst. It potentially absorbs a high fraction (approximately 13.5%) of the solar spectrum [14]. However, the low electron mobility, the short lifetime of light-induced charge carriers (~10 ps), and short hole diffusion length (~2–4 nm) limit the photoconversion activities of free-standing hematite species [15]. In addition,  $\alpha\text{-Fe}_2\text{O}_3$  has a higher positive CB state potential than  $\text{H}^+/\text{H}_2$  (0 V vs. normal hydrogen electrode (NHE)), making it unsuitable for  $\text{H}_2$  production. An interesting approach to addressing these fundamental challenges is fabricating a direct Z-scheme heterojunction platform where  $\alpha\text{-Fe}_2\text{O}_3$  suitably serves as a PC II entity [16]. In particular, the 2D [001]-cut layered  $\alpha\text{-Fe}_2\text{O}_3$  has been explored as an active site for photocatalytic applications because of its high charge carrier mobility. Nitrogen-doped graphene is a promising PC I for a suitable 2D  $\alpha\text{-Fe}_2\text{O}_3$ -contained Z-scheme system. Graphene (Gr), a typical 2D sheet feature containing an extreme  $\pi$ -conjugated system, is a semimetal with a zero bandgap, excellent conductivity, and high electron transferability [17]. Furthermore, it exhibits a large surface area and desirable chemical stability, making it preferable for photocatalysis. On the other hand, the electronic properties of graphene can significantly be modulated by doping it with n-type dopants (e.g., nitrogen (N) atoms) [18]. The Fermi position in the nitrogen-doped graphene (NGr) is shifted to the VB level, demonstrating that NGr functions as an n-type semiconductor [19]. Each N-atom contributes an excess electron delocalized over the entire plane while the NGr retains its flat structure and excellent conductivity. The as-obtained 2D NGr exhibits a visible range bandgap of 2.2–2.4 eV with a negative CB potential (vs. NHE) [20], which is advantageous for hydrogen production. Thus, as a PC I entity, it can be combined with hematite in a 2D/2D direct Z-scheme  $\alpha\text{-Fe}_2\text{O}_3$  @NGr core-shell system. However, the conventional binary Z-scheme systems continue to perform poorly. On the other hand, anchoring metal cocatalysts on the surface of photocatalysts is another effective strategy for promoting charge carrier transfer and providing more active sites. In this picture, platinum (Pt)-containing entities are widely identified as the most effective cocatalysts for the PHE application. The Pt species generally provide suitable Fermi levels and low potentials for PHE reactions [21]. Unfortunately, satisfactory Pt-like activity for all assembled atoms has been infrequently attained [22]. Compared to Pt nanoparticles (NPs), single-atoms (SAs) provide significant advantages [23]. The Pt SA cocatalysts may be fully dispersed (100%) on a photocatalyst surface [24]. The strong SA-host electronic interactions also promote charge carrier transfer. In addition, a SA entity often exposes a well-defined coordination environment. As a result, the Pt SA cocatalysts are very convenient for improving atom-utilization efficiency and maximizing catalytic activities. It is noteworthy that the presence of electron-rich N atoms in the 2D N-containing carbon supports is favorable for loading the Pt SA catalysts [19,25]. The implantation of Pt SA cocatalysts into the 2D carbon-related structures, in particular, can significantly accelerate in-plane charge carrier transfer and utilization, thus improving the catalyst activity for the entire system [26].

This work introduced the appropriate way to create a high-active three-component system:  $\alpha\text{-Fe}_2\text{O}_3$  @NGr<sub>3</sub>–Pt<sub>SAs</sub>. The prototypical three-component design resulted in an excellent performance in PHE compared to their parents and outperformed currently reported catalysts for PHE activity under visible light. The new system works based on an advanced direct Z-scheme mechanism where the  $\alpha\text{-Fe}_2\text{O}_3$  acts as PC II, NGr as PC I, and Pt<sub>SAs</sub> as cocatalyst to beat the shortcomings of its individual catalysts in the PHE activity. It is noted that the formation of Pt SAs into NGr can be considered a case of doping. According to this view, the changes in the optoelectronic and structural properties of the host (e.g., NGr) induced by doping with Pt SAs have been systematically investigated. The critical point is that the Pt SAs are good cocatalysts that can improve catalytic reactions. Furthermore, the catalysts deriving from the experimental activity have been investigated theoretically by

density functional theory (DFT) and finite-difference time-domain (FDTD) approaches based on knowledge of the structure and electronic, optical, chemical, and catalytic properties of  $\alpha\text{-Fe}_2\text{O}_3$ , NGr, and Pt single atoms catalysts, and their role in catalytic reactions. Integrating experimental and theoretical investigations allows us to provide clear evidence of the mechanism based on the excellent performance of the new catalyst.

## 2. Experimental section

### 2.1. Preparation of 2D hexagonal $\alpha\text{-Fe}_2\text{O}_3$

Hematite ( $\alpha\text{-Fe}_2\text{O}_3$ ) was hydrothermally synthesized following steps outlined in a prior report [27] with appropriate adjustments to achieve the ideal hexagonal structures. To begin,  $\text{FeCl}_3\cdot 6\text{H}_2\text{O}$  (0.1 g),  $\text{NaCH}_3\text{COO}$  (0.5 g), and PVP (1.5 g) were added to 40 mL of distilled water and agitated for 2 h at 60 °C until a homogeneous solution was produced. The resultant solution was then placed in a Teflon-lined stainless-steel autoclave and heated at 180 °C for 24 h. The precipitates were centrifuged and washed with water and ethanol after natural cooling to isolate the clear red powder of hexagonal  $\alpha\text{-Fe}_2\text{O}_3$  NPs. Before further use, the finished sample was calcined in air at 800 °C for 2 h.

### 2.2. Preparation of binary 2D/2D $\alpha\text{-Fe}_2\text{O}_3$ @NGr samples

In 50 mL of distilled water containing suitable proportions of glucose and dicyandiamide, 0.1 g of as-obtained  $\alpha\text{-Fe}_2\text{O}_3$  powder was added (DCDA). The resultant suspension was sonicated at room temperature for 30 min before being frozen for 4 h and dried for 48 h. The finished product was pyrolyzed in argon at 800 °C for 2 h to produce black  $\alpha\text{-Fe}_2\text{O}_3$  @NGr nanohybrid materials. NGr shell thicknesses of 1, 3, and 7 nm were achieved by altering the additional amounts of glucose and DCDA precursors by 10–20, 20–30, and 40–60 mg, and the corresponding core-shell entities were called  $\alpha\text{-Fe}_2\text{O}_3$  @NGr<sub>1</sub>,  $\alpha\text{-Fe}_2\text{O}_3$  @NGr<sub>3</sub>, and  $\alpha\text{-Fe}_2\text{O}_3$  @NGr<sub>7</sub>, respectively.

### 2.3. Preparation of ternary 2D/2D $\alpha\text{-Fe}_2\text{O}_3$ @NGr<sub>3</sub>–Pt samples

First, 0.1 g of as-obtained  $\alpha\text{-Fe}_2\text{O}_3$  powder was added to 50 mL of distilled water containing desirable amounts of 20 mg of glucose and 30 mg of DCDA. Next, to obtain  $\alpha\text{-Fe}_2\text{O}_3$  @NGr<sub>3</sub>–Pt<sub>SAs</sub>, 0.03 mL of Pt<sup>4+</sup> stock (1 g  $\text{H}_2\text{PtCl}_6\cdot 6\text{H}_2\text{O}$  in 20 mL of water) was added to the solution above. The following freezing, freezing-drying, and pyrolyzing procedures were repeated with the  $\alpha\text{-Fe}_2\text{O}_3$  @NGr<sub>3</sub> preparation to produce  $\alpha\text{-Fe}_2\text{O}_3$  @NGr<sub>3</sub>–Pt<sub>SAs</sub> with a Pt loading of 0.5 wt%. To obtain  $\alpha\text{-Fe}_2\text{O}_3$  @NGr<sub>3</sub>–Pt<sub>NPs</sub>, 0.12 mL of Pt<sup>4+</sup> stock was utilized. The resultant solution was mixed for 30 min before being oven-dried for 18 h at 50 °C. Finally, the powder was pyrolyzed in argon at 800 °C for 2 h to produce  $\alpha\text{-Fe}_2\text{O}_3$  @NGr<sub>3</sub>–Pt<sub>NPs</sub> with a Pt loading of 2.0 wt%.

## 2.4. Characterization

The morphological properties of the samples were investigated using spherical aberration-corrected transmission electron microscopy (TEM; JEM-2010 microscope, JEOL). The crystalline structures were measured using X-ray diffraction (XRD; D/Max 2005, Rigaku) with Cu K $\alpha$  radiation ( $\lambda = 1.54178 \text{ \AA}$ ). The absorption spectra of the obtained suspensions were analyzed using ultraviolet-visible diffuse reflection spectroscopy (UV-vis DRS) at room temperature. The surface chemical states of the elements in the prepared photocatalysts were studied using X-ray photoelectron spectroscopy (XPS; Multilab 2000 instrument, Thermo Fisher Scientific) with monochromated Al K $\alpha$  radiation ( $h\nu = 1486.6 \text{ eV}$ ). The C 1 s peak located at around 285 eV was used to calibrate the binding energies. Ultraviolet photoelectron spectroscopy (UPS) was also performed using a monochromatic Al K $\alpha$  X-ray source ( $h\nu = 1486.6 \text{ eV}$ ) and a helium discharge lamp ( $h\nu = 21.2 \text{ eV}$ ). The result

was calibrated by referencing to the Fermi edge of Ag. The specific surface areas of the samples were examined via the nitrogen gas adsorption/desorption techniques to produce high-quality data through the Brunauer–Emmett–Teller (BET) method using a Micromeritics Tristar 3000 analyzer. The Raman spectra of samples were studied by a LabRam ARAMIS IR2 spectrometer. Electron spin resonance (ESR) spectra were conducted on a JEOL JES-X320 system. A typical DMPO- $\bullet\text{O}_2$  ESR analysis was performed under visible light irradiation in a saturated O<sub>2</sub> containing methanol and 5, 5-dimethyl-1-pyrroline Noxide (DMPO) working as a spin trapping. Steady-state photoluminescence (PL) and time-resolved photoluminescence (TRPL) were performed at room temperature under pulsed excitation of the laser diode (excitation wavelength = 374 nm and pulse width = 1.0 ps). For this aim, the photocatalysts are deposited on glass substrates. The excitation beam was focused on the samples via double grating (1200 groove/mm), and the emission light was collected via single grating (1200 groove/mm). The resulting signals were analyzed by a single-photon counting in 200–870 nm. The TRPL decay times were calculated through DAS 6 analyses (Fluorolog 3 with TCSPC, HORIBA SCIENTIFIC).

## 2.5. Photoelectrochemical measurements

For this purpose, the catalysts were spray-deposited on the carbon cloth substrate (1 cm × 1 cm) with a microporous layer. Linear sweep voltammetry (LSV) was investigated using a three-electrode setup (Gamry Instruments Reference 3000, Potentiostat/Galvanostat/ZRA) with and without visible light irradiation from a 300 W xenon lamp (Asahi, Max 303). LSV polarizations were recorded at a sweep rate of 20 mV s<sup>-1</sup> from –0.3–0.7 V (vs. SCE) recorded in N<sub>2</sub>-saturated 0.1 M Na<sub>2</sub>SO<sub>4</sub> electrolyte. Transient photocurrent–time characteristics (I–t curve) were recorded at a bias voltage of 0.2 V in N<sub>2</sub>-saturated 0.1 M Na<sub>2</sub>SO<sub>4</sub> electrolyte under chopped light irradiation. Electrochemical impedance spectroscopy (EIS) was also conducted in N<sub>2</sub>-saturated 0.1 M Na<sub>2</sub>SO<sub>4</sub> electrolyte at 25 °C from 100 kHz to 0.05 Hz. The working electrolyte was purged with pure N<sub>2</sub> to prevent any attack from oxygen during the photoelectrochemical tests.

## 2.6. Photocatalytic hydrogen evolution

The PHE activity for the as-obtained photocatalysts was experimentally performed under visible light irradiation. For this aim, 50 mg of each photocatalyst was dispersed in a 50 mL mixture of 0.25 M Na<sub>2</sub>SO<sub>3</sub> and 0.25 M Na<sub>2</sub>S solutions as the sacrificial hole reagent. Before the visible light irradiation ( $\lambda > 420$  nm) with a 300 W xenon lamp (Asahi, Max 303), the reaction solution was stirred under dark conditions for 1 h to achieve the adsorption/desorption equilibrium of the reactants on the photocatalyst's surface. At the same time, pure nitrogen was injected to the reaction solution to remove the air. The PHE reaction time for each cycle was set as 4 h. As each cycle was completed, the photocatalysts were isolated by centrifugation and air-dried at 100 °C for 2 h before reusing. The as-evolved hydrogen gas was analyzed with a gas chromatograph (Shimadzu, GC-2010). For comparison, the PHE activity was also performed under sunlight irradiation.

## 2.7. FDTD simulations

The 2D/3D total-field/scattered-field (TFSF) Finite-Difference Time-Domain (FDTD) (Ansys Lumerial FDTD) simulation was used to calculate the spatial distribution of electric intensity near the photocatalyst surface of a free 2D hexagonal α-Fe<sub>2</sub>O<sub>3</sub>, binary 2D hexagonal α-Fe<sub>2</sub>O<sub>3</sub> @NGr<sub>3</sub>, and ternary α-Fe<sub>2</sub>O<sub>3</sub> @NGr<sub>3</sub>–Pt<sub>SAs</sub>. In the simulation, the TFSF source was a plane-wave pulse. Frequency-domain field monitor obtained the electric intensity. The spatial resolution in 2D FDTD simulation for α-Fe<sub>2</sub>O<sub>3</sub> and 2D α-Fe<sub>2</sub>O<sub>3</sub> @NGr<sub>3</sub> was set to 1.7 nm. In the case of α-Fe<sub>2</sub>O<sub>3</sub> @NGr<sub>3</sub>–Pt<sub>SAs</sub>, the spatial resolution was set to 0.0125 nm to

represent the localized surface plasmon effect at the small Pt with a radius of 0.25 nm.

## 2.8. DFT calculations

The calculations were performed at the level of Density Functional Theory (DFT), as implemented in VASP 6.1.1 code [28]. The valence electrons used for each atom were recommended in the VASP website, H (1 s), C (2 s<sup>2</sup>2p<sup>2</sup>), N (2 s<sup>2</sup>2p<sup>3</sup>), Fe (4 s<sup>1</sup>3d<sup>7</sup>), O (2 s<sup>2</sup>2p<sup>4</sup>), and Pt (5 s<sup>1</sup>d<sup>9</sup>) which have been expanded on a set of plane waves with a kinetic cut-off of 400 eV. In contrast, the core electrons were treated with the Projector Augmented Wave (PAW) approach [29]. The Perdew–Burke–Ernzerhof (PBE) exchange–correlation functional [30] was used with a Hubbard [31] correction of U = 4 for α-Fe<sub>2</sub>O<sub>3</sub> [32]. The truncation criteria for electronic and ionic loops were set to 10<sup>-6</sup> eV and –10<sup>-3</sup> eV/Å, respectively. The reciprocal space has been sampled by adopting a 5 × 5 × 3 grid for the α-Fe<sub>2</sub>O<sub>3</sub> bulk material and decreased to the gamma point for the surfaces and interface calculation, due to the large dimension of the cells. Dispersion forces have been considered according to the Grimme's D3 parametrization scheme [33]. To model Nitrogen doped-graphene (NGr), a nitrogen-dopant concentration of about 4% was considered in all models, similar to that found experimentally. Solvent effects were not included in our models. However, we recently showed that for SA catalysts based on transition metal atoms stabilized in NGr, the effect of the solvent on the energetics of the PHE is negligible, being of the order of 0.04 eV.

## 3. Results and discussion

### 3.1. Material characterizations

**Fig. S1 (Supplementary Material)** depicts the two-step preparation of three-factored 2D/2D α-Fe<sub>2</sub>O<sub>3</sub> @NGr–Pt<sub>SAs</sub> core-shell fabrication. The 2D hexagonal α-Fe<sub>2</sub>O<sub>3</sub> is generated hydrothermally via an autoclave-made technique and then enclosed by the 2D NGr–Pt<sub>SAs</sub> shell by pyrolysis. The encapsulated NGr shell thickness is optimized, and samples containing free graphene (Gr), NGr, and NGr–Pt<sub>SAs</sub> are also generated for comparison (see **Supplementary Material**). **Fig. 1a** shows TEM images of as-calcined hematite, with three α-Fe<sub>2</sub>O<sub>3</sub> entities indicating uniform and hexagonal nanoplate structures with lateral diameters of ≈ 55 and 65 nm. The selected area electron diffraction (SAED) pattern in **Fig. 1a**'s inset describes that the as-obtained 2D α-Fe<sub>2</sub>O<sub>3</sub> species are single crystalline. **Fig. S2** depicts their elemental maps. **Fig. S3** presents high-resolution TEM images of the as-prepared free NGr entity, in which the atomic content of the N dopant is ≈ 3.5%. **Fig. S4–S6** is the 2D/2D α-Fe<sub>2</sub>O<sub>3</sub> @NGr core-shell structures with thicknesses of ≈ 1, 3, and 7 nm. The corresponding samples are denoted as α-Fe<sub>2</sub>O<sub>3</sub> @NGr<sub>1</sub>, α-Fe<sub>2</sub>O<sub>3</sub> @NGr<sub>3</sub>, and α-Fe<sub>2</sub>O<sub>3</sub> @NGr<sub>7</sub>. The α-Fe<sub>2</sub>O<sub>3</sub> @NGr<sub>1</sub> species exposes a partially uncovered α-Fe<sub>2</sub>O<sub>3</sub> surface, whereas the NGr<sub>7</sub>-containing one exposes a uniformly thin NGr shell. It is also worth noting that the versatile NGr in these samples can function as both a shell to enclose α-Fe<sub>2</sub>O<sub>3</sub> and a network to inhibit the aggregation of α-Fe<sub>2</sub>O<sub>3</sub> @NGr species. **Fig. 1b** depicts as-pyrolyzed α-Fe<sub>2</sub>O<sub>3</sub> @NGr<sub>3</sub>–Pt<sub>SAs</sub> core-shell nanohybrids with a 2D/2D model inset sitting on the NGr network. A 3-nm NGr<sub>3</sub>–Pt<sub>SAs</sub> shell covers the α-Fe<sub>2</sub>O<sub>3</sub> surface, and the lattice distance of the NGr(002) shell is roughly 0.32 nm, according to high-resolution TEM (**Fig. 1c**). **Figs. 1d** and **1e** shows the intensity profile of the selected-area plot as well as the appropriate structural model of a clean-surface free-standing α-Fe<sub>2</sub>O<sub>3</sub>(104) and NGr<sub>3</sub>(002) shell. The equivalent lattice distances of the α-Fe<sub>2</sub>O<sub>3</sub>(104) and NGr<sub>3</sub>(002) planes are 0.27 and 0.32 nm, respectively. **Fig. 1f** presents a high-angle annular dark-field scanning transmission electron microscopy (HAADF-STEM) image of NGr<sub>3</sub>–Pt<sub>SAs</sub>(002) shell over α-Fe<sub>2</sub>O<sub>3</sub> using the probe Cs corrector, in which the successful formation of the isolated Pt atoms dispersed on the NGr shell was indicated by the white arrows. The selected highlighted area profile supports the atomic implantation of Pt

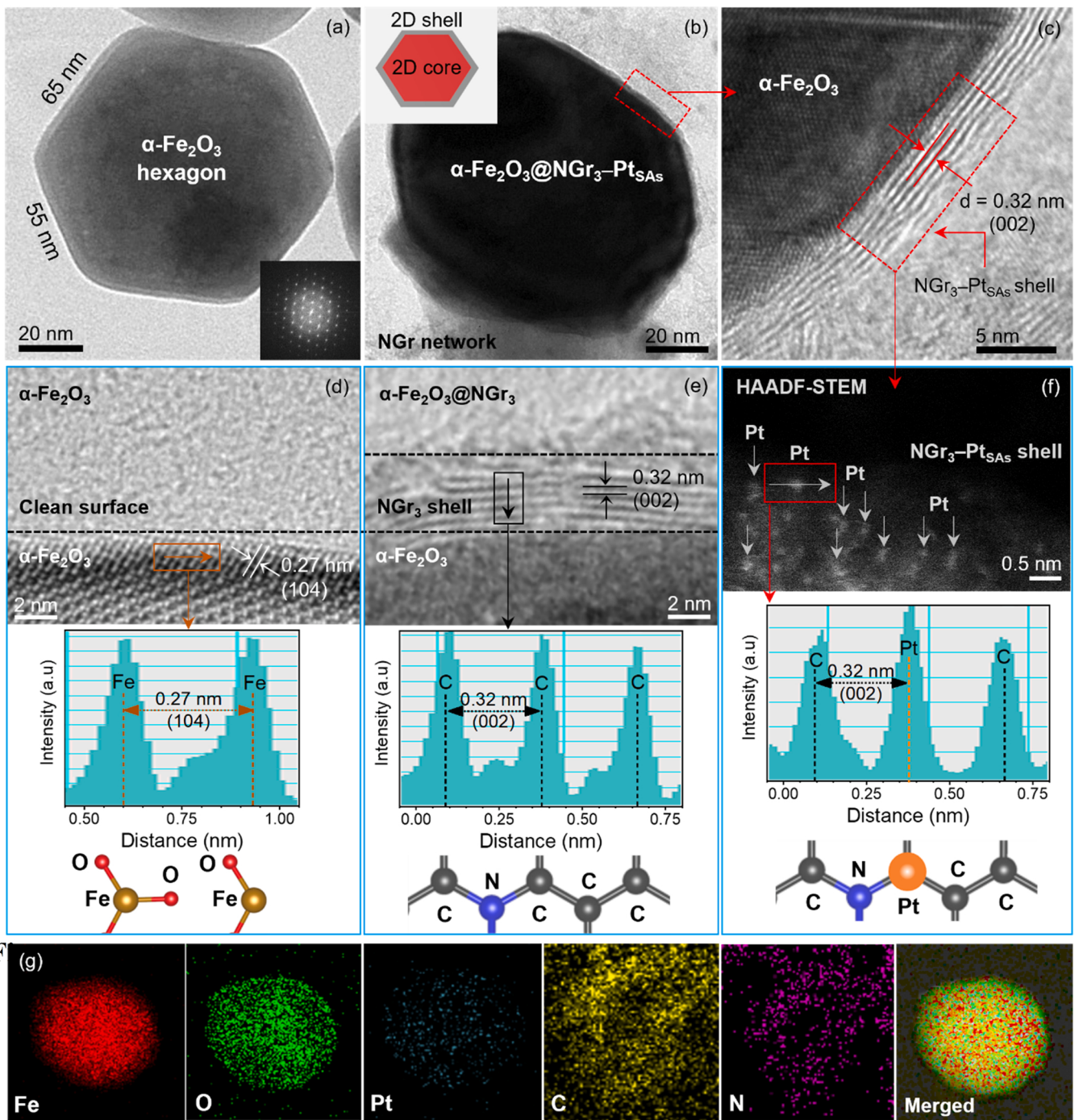


**Fig. 1.** (a) HAAADF-STEM image including SAED pattern of as-calcined free-standing hexagonal  $\alpha\text{-Fe}_2\text{O}_3$ . (b) TEM image of as-pyrolyzed  $\alpha\text{-Fe}_2\text{O}_3@NGr_3\text{-Pt}_{SAs}$  core@shell nanohybrids with possible modeling given in the inset, (c) high-resolution TEM observation for NGr-Pt<sub>SAs</sub> hybridized over  $\alpha\text{-Fe}_2\text{O}_3@NGr_3\text{-Pt}_{SAs}$  surface. Surface observation and the selected-area intensity profiles with the corresponding structural modeling of (d) as-calcined free-standing hexagonal  $\alpha\text{-Fe}_2\text{O}_3(104)$ , (e) NGr<sub>3</sub>(002) shell over  $\alpha\text{-Fe}_2\text{O}_3$ , and (f) Typical high resolution high-angle annular dark-field scanning transmission electron microscopy (HAADF-STEM) image of NGr<sub>3</sub>-Pt<sub>SAs</sub>(002) shell over  $\alpha\text{-Fe}_2\text{O}_3$  in which the white arrows represent the isolated Pt atoms decorating the NGr shell. (g) TEM-EDS elemental map of Fe (red), O (green), Pt (cyan), C (yellow), N (pink), and their elemental merge in  $\alpha\text{-Fe}_2\text{O}_3@NGr_3\text{-Pt}_{SAs}$  nanohybrids.

SAs in the NGr shell matrix without affecting the host lattice distance. Fig. 1 g shows the energy-dispersive X-ray spectroscopy (EDS) maps of  $\alpha\text{-Fe}_2\text{O}_3@NGr_3\text{-Pt}_{SAs}$ . The coexistence of Fe, O, Pt, C, and N elements are detected in red, green, cyan, yellow, and pink, respectively, which also demonstrates the atomically dispersed Pt SAs in the three-factored core-shell system. In addition, the presence of isolated Pt SAs in the as-obtained binary NGr-Pt<sub>SAs</sub> sample is also confirmed by the HAADF-STEM technique, as shown in Fig. S7. A dense white dot further

represents the successful formation of isolated Pt SAs in the binary NGr-Pt<sub>SAs</sub> entity (Fig. S7a), which is confirmed by EDS maps and spectrum (Fig. S7b and 7c). The advantages of the freeze-drying process followed by pyrolysis in preparing single-atom catalyst-supported carbon-hosted materials were reported in our previous work. Accordingly, the former freeze-drying step favored well-disperse  $\text{Pt}^{4+}$  species in the NGr-precursor network. Then, the presence of N dopants in the NGr network favorably helps to reduce metallic ions to their single-atom

form during the latter pyrolysis process. The presence of Pt NPs in ternary  $\alpha\text{-Fe}_2\text{O}_3 @\text{NGr}_3\text{-Pt}_{\text{SAs}}$  is further confirmed in Fig. S8 (Supplementary Material).

The hexagonal structure of  $\alpha\text{-Fe}_2\text{O}_3$  nanoplates is further observed by FESEM technique (Fig. 2a). Fig. 2b describes the FESEM image of free NGr with a multilayered structure and high-porosity surface. After the surface-hybridization, the  $\alpha\text{-Fe}_2\text{O}_3$  nanoplates are randomly covered with the  $\text{NGr}_3\text{-Pt}_{\text{SAs}}$ , likely generating the  $\alpha\text{-Fe}_2\text{O}_3 @\text{NGr}_3\text{-Pt}_{\text{SAs}}$  core-shell entities with the thickness of  $\approx 10$  nm sitting on the NGr network, as depicted in Fig. 2c. The specific surface area of free-standing hexagonal  $\alpha\text{-Fe}_2\text{O}_3$ , binary  $\alpha\text{-Fe}_2\text{O}_3 @\text{NGr}_3$  core-shell, and ternary  $\alpha\text{-Fe}_2\text{O}_3 @\text{NGr}_3\text{-Pt}_{\text{SAs}}$  nanohybrids is investigated utilizing nitrogen adsorption/desorption isotherms and the BET measurements. After surface-hybridization with NGr-containing species, the performance of free  $\alpha\text{-Fe}_2\text{O}_3$  nanoplates, which have a relatively low nitrogen adsorption/desorption capability, can be significantly increased (Fig. 2d). Furthermore, the sublimation of ice crystals during the nanocomposite materials' freeze-drying process is anticipated to result in high-porosity nanostructures. As a result, the massive BET surface areas of binary  $\alpha\text{-Fe}_2\text{O}_3 @\text{NGr}_3$  ( $117 \text{ m}^2 \text{ g}^{-1}$ ) and ternary  $\alpha\text{-Fe}_2\text{O}_3 @\text{NGr}_3\text{-Pt}_{\text{SAs}}$  ( $121 \text{ m}^2 \text{ g}^{-1}$ ) nanocomposites are determined, which are much greater than that of free-existing hexagonal  $\alpha\text{-Fe}_2\text{O}_3$  nanoplates ( $16 \text{ m}^2 \text{ g}^{-1}$ ). Thus, many catalytical sites for PHE reactions are predicted to be exposed over the NGr-containing entities.

On the other hand, Fig. S9a shows the XRD pattern of free-standing  $\alpha\text{-Fe}_2\text{O}_3$  (red curve). The diffraction peaks observed at  $24.20$ ,  $33.25$ ,  $35.65$ ,  $40.95$ ,  $49.55$ , and  $54.14^\circ$ , respectively, correspond to the  $(012)$ ,  $(104)$ ,  $(110)$ ,  $(113)$ ,  $(024)$ , and  $(116)$  crystalline planes of the rhombohedral structure of  $\text{Fe}_2\text{O}_3$  (JCPDS No. 86–0550). In the NGr (grey curve) case, the prominent diffraction peak was found at about  $26.20^\circ$ . In the ternary  $\alpha\text{-Fe}_2\text{O}_3 @\text{NGr}_3\text{-Pt}_{\text{SAs}}$ , the XRD peaks of  $\alpha\text{-Fe}_2\text{O}_3$  and NGr ingredients could be detectable; however, the intensity of the NGr diffraction peak is low, possibly due to its low-content hybridization on the hematite host. In contrast, the absence of the Pt phase in XRD measuring demonstrated the full dispersion nature of Pt single-atoms form on the surface of  $\alpha\text{-Fe}_2\text{O}_3 @\text{NGr}_3$  support. As described in Fig. S9b, the right shift in the XRD peaks for  $\alpha\text{-Fe}_2\text{O}_3 @\text{NGr}_3\text{-Pt}_{\text{SAs}}$  entity is confirmed for  $(104)$  and  $(110)$  peaks compared to free-standing  $\alpha\text{-Fe}_2\text{O}_3$ . In fact, the coating of NGr on  $\alpha\text{-Fe}_2\text{O}_3$  can result in the transfer of the electrons from the NGr to  $\alpha\text{-Fe}_2\text{O}_3$  component, reducing  $\text{Fe}^{3+}$

to  $\text{Fe}^{2+}$  species and the Fe-N bond between the N site in NGr and Fe site in  $\alpha\text{-Fe}_2\text{O}_3$  is also appeared in the composites (as verified by XPS analysis below), which possibly lead to the right shift in their XRD peaks position.

The Raman spectra of Gr and NGr species are shown in Fig. 3a, with the two peaks of the D band and G band clearly visible. The intensity ratio of the D band to the G band ( $I_D/I_G$ ) is often used to assess the graphene disorder degree. As shown in the figure, the resulting NGr has a higher  $I_D/I_G$  1.10 than the free Gr entity (1.06), implying that the doped graphene has more defects than the pristine one. Furthermore, the shift in the D and G band positions in Gr and NGr samples (inset of Fig. 3a) suggests that N dopant intercalation into the conjugated carbon backbone can partially cause disordered structures by breaking the  $\text{sp}^2$  C six-member rings to form the  $\text{sp}^3$  C five-member pyrrolic N bonding configuration [34]. The presence of numerous defects and N atoms in the resulting 2D NGr may boost its photocatalytic activity [5,19]. The chemical states of  $\alpha\text{-Fe}_2\text{O}_3$ , NGr,  $\alpha\text{-Fe}_2\text{O}_3 @\text{NGr}_3$ , and  $\alpha\text{-Fe}_2\text{O}_3 @\text{NGr}_3\text{-Pt}_{\text{SAs}}$  samples are characterized by high-resolution XPS, as shown in Fig. S10(a-d) (Supplementary Material). The coexistence of the Fe, O, C, N, and Pt elements in each sample is detected, respectively, indicating the high purity of the samples. As the core photocatalytic constituents of these designs, the core levels of  $\text{Fe} 2\text{p}$ ,  $\text{Pt} 4\text{f}$ , and  $\text{N} 1\text{s}$  are further analyzed. Fig. 3b shows a characteristic peak of  $\text{Fe}^{3+}$  with a main  $\text{Fe} 2\text{p}_{3/2}$  component and a shakeup satellite at  $709.4$  and  $718.0$  eV for  $\alpha\text{-Fe}_2\text{O}_3$ . Actually, the surface decoration of a NGr shell on  $\alpha\text{-Fe}_2\text{O}_3$  possibly induces the transfer of the electrons from the NGr to  $\alpha\text{-Fe}_2\text{O}_3$  component, then reducing  $\text{Fe}^{3+}$  to  $\text{Fe}^{2+}$  species. Thus, it gives rise to the  $\text{Fe}^{2+}$  concentration, and the intensity of the shakeup satellite peaks in  $\text{Fe} 2\text{p}$  XPS spectra decreases over the NGr-containing composites. From the XPS fitting results of  $\text{Fe} 2\text{p}$  level (Fig. S11), the relevant concentration of  $\text{Fe}^{2+}$  is  $6.8\%$ ,  $16.7\%$ , and  $17.3\%$  for free  $\alpha\text{-Fe}_2\text{O}_3$ , binary  $\alpha\text{-Fe}_2\text{O}_3 @\text{NGr}_3$ , and ternary  $\alpha\text{-Fe}_2\text{O}_3 @\text{NGr}_3\text{-Pt}_{\text{SAs}}$ , respectively. In addition, the appearance of Fe-N bond further suggests the strong coordination interaction between NGr and  $\alpha\text{-Fe}_2\text{O}_3$  (as illustrated in Fig. 3d below). This all results in positive shifting in the position of the XPS  $\text{Fe} 2\text{p}$  peaks in the binary ( $\alpha\text{-Fe}_2\text{O}_3 @\text{NGr}_3$ ) and ternary ( $\alpha\text{-Fe}_2\text{O}_3 @\text{NGr}_3\text{-Pt}_{\text{SAs}}$ ) as compared with the parent  $\alpha\text{-Fe}_2\text{O}_3$ . Fig. 3c shows the XPS-fitted core level of  $\text{Pt} 4\text{f}$ , where most Pt species are metal  $\text{Pt}^0$ , while a small amount of them are oxidized as  $\text{Pt}^{2+}$  component. The presence of N dopant in NGr host can favorably reduce the Pt ion to its metal form [35]. The high-resolution  $\text{N} 1\text{s}$  XPS is fitted into four peaks (Fig. 3d) at  $398.0$ ,  $399.5$ ,  $400.8$ , and  $403.1$  eV matching with pyridinic N, pyrrolic N, graphitic N, and oxidized N species, respectively. The oxidized N peak here further reveals the coordination interaction between the N sites and Fe species in  $\alpha\text{-Fe}_2\text{O}_3$  and the N sites and Pt SAs cocatalyst, enhancing the nature of electronic interactions between the three constituents in the ternary  $\alpha\text{-Fe}_2\text{O}_3 @\text{NGr}_3\text{-Pt}_{\text{SAs}}$  system fabricated. In addition, the XPS of  $\text{N} 1\text{s}$  of NGr and  $\alpha\text{-Fe}_2\text{O}_3 @\text{NGr}_3$  is added for comparison (Fig. S12a and S12b). As can be seen, the high-resolution  $\text{N} 1\text{s}$  XPS for free NGr is mainly composed of three peaks: pyridinic N, pyrrolic N, and graphitic N entities, respectively. In contrast, the presence of the oxidized N peaks in binary sample indicated the formation of Fe-N bridge between NGr and  $\alpha\text{-Fe}_2\text{O}_3$  components. It is noted that the appearance of Fe-N bindings can possibly lead to negatively shift in the peak position of N species (e.g., pyridinic N) compared to that of free NGr. UV-vis DRS is used to assess the optical properties of  $\alpha\text{-Fe}_2\text{O}_3$ , NGr, and  $\alpha\text{-Fe}_2\text{O}_3 @\text{NGr}_3$  species. Fig. 3e shows that the free-standing  $\alpha\text{-Fe}_2\text{O}_3$  and NGr photocatalysts absorb visible light and have cut-off wavelengths of  $602\text{ nm}$  and  $587\text{ nm}$ . Using the Tauc equation, the equivalent bandgap energy for  $\alpha\text{-Fe}_2\text{O}_3$  and NGr is calculated to be  $2.06\text{ eV}$  and  $2.11\text{ eV}$ , respectively. While the  $\alpha\text{-Fe}_2\text{O}_3 @\text{NGr}_3$  hybrid had a cut-off wavelength of  $594\text{ nm}$  (bandgap of  $2.09\text{ eV}$ ), showing a stronger light absorption ability and a redshift of the semiconductor-graphene-related system compared to free-standing hematite that was entirely consistent with previous studies. Using the empirical equation ( $\text{CBM} = X - \frac{1}{2}\text{E}_g$ , where  $X$

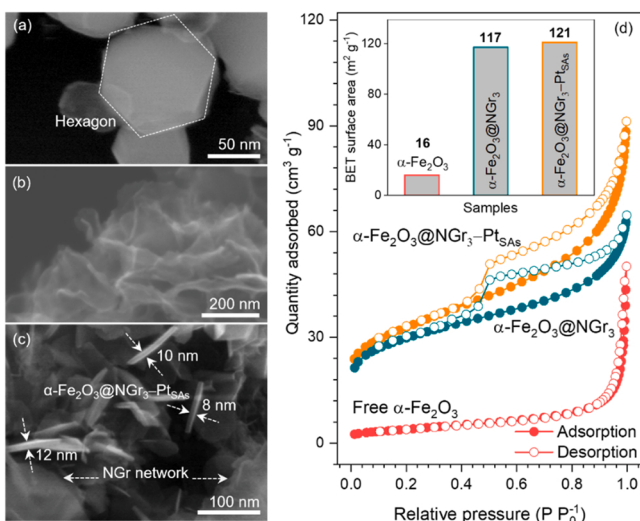


**Fig. 2.** FESEM images of (a) hexagonal  $\alpha\text{-Fe}_2\text{O}_3$  nanoplates, (b) free-standing NGr, and (c) ternary  $\alpha\text{-Fe}_2\text{O}_3 @\text{NGr}_3\text{-Pt}_{\text{SAs}}$  core-shell species sitting on NGr network. (d) Nitrogen adsorption/desorption isotherms characterization and relative BET-specific surface area for free-standing  $\alpha\text{-Fe}_2\text{O}_3$ , binary  $\alpha\text{-Fe}_2\text{O}_3 @\text{NGr}_3$ , and ternary  $\alpha\text{-Fe}_2\text{O}_3 @\text{NGr}_3\text{-Pt}_{\text{SAs}}$  fabrications.

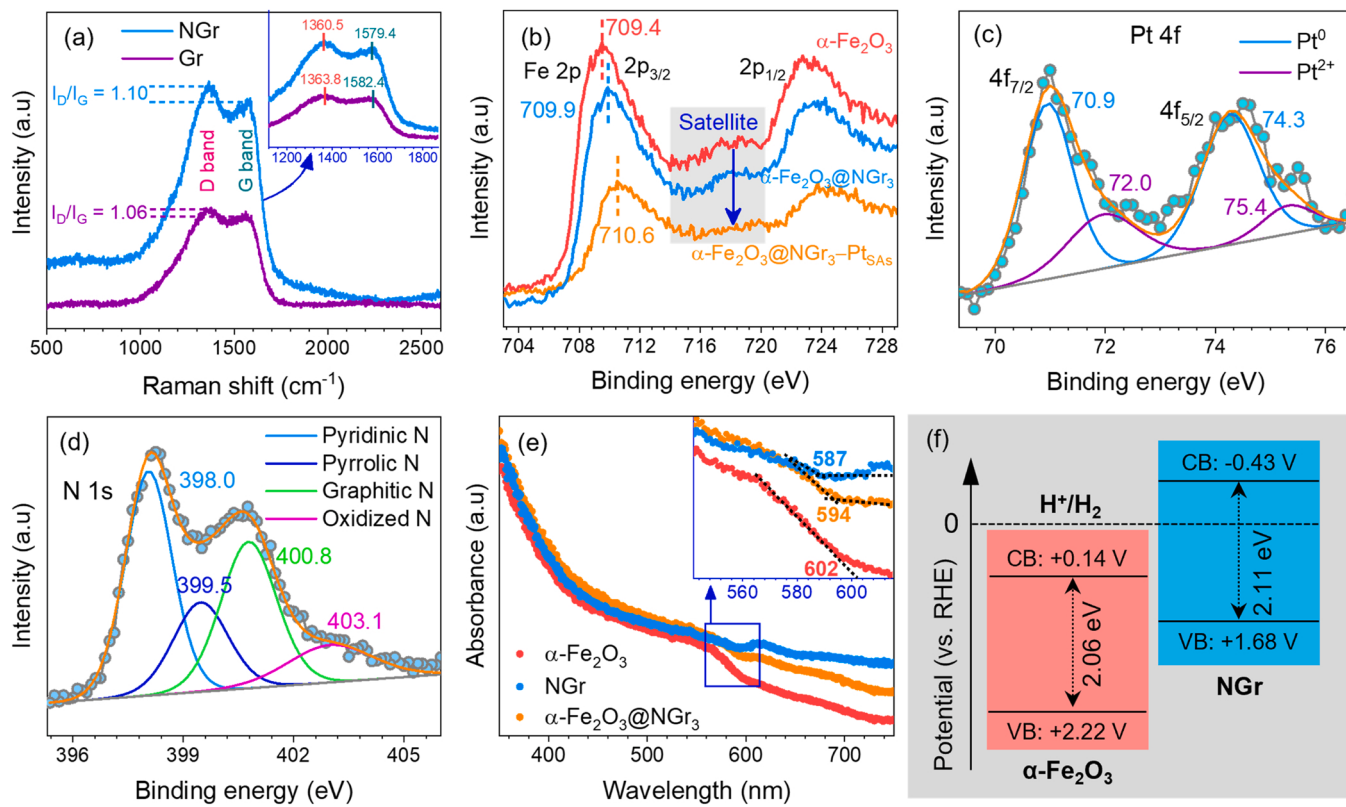


**Fig. 3.** (a) Raman spectra of pristine graphene (Gr) and nitrogen-doped graphene (NGr), inset:  $I_D/I_G$  ratio and change in the position of D and G bands. XPS core-level spectra of (b) Fe 2p in free-standing  $\alpha\text{-Fe}_2\text{O}_3$ , binary  $\alpha\text{-Fe}_2\text{O}_3$  @NGr<sub>3</sub>, and ternary  $\alpha\text{-Fe}_2\text{O}_3$  @NGr<sub>3</sub>-Pt<sub>SAs</sub>; (c) Pt 4 f and (d) N 1 s in ternary  $\alpha\text{-Fe}_2\text{O}_3$  @NGr<sub>3</sub>-Pt<sub>SAs</sub>; (e) UV-vis DRS spectra of  $\alpha\text{-Fe}_2\text{O}_3$ , NGr, and binary  $\alpha\text{-Fe}_2\text{O}_3$  @NGr<sub>3</sub>; and their corresponding cut-off wavelengths in the inset. (f) Relevant energy band potentials alignment between  $\alpha\text{-Fe}_2\text{O}_3$  (PC II) and NGr (PC I) constituents in a direct Z-scheme construction.

(5.825 eV) is the absolute electronegativity of  $\alpha\text{-Fe}_2\text{O}_3$  and  $E_g$  is the bandgap energy), the CBM and VBM of  $\alpha\text{-Fe}_2\text{O}_3$  are calculated to be 4.80 and 6.86 eV. From the UPS measurement (Fig. S13), the VBM value of NGr is 6.10 eV by subtracting the width of the He I UPS spectrum at the excitation energy (21.2 eV). The CBM is found to be 3.99 eV from  $VBM - E_g$  [36]. According to the reference standard, which equals  $-4.44$  eV against vacuum level for 0 V vs. NHE (normal hydrogen electrode), the CBM values in electron volts are converted to the electrochemical energy potentials in volts, which are  $+0.36$  and  $-0.45$  V vs. NHE, respectively (Fig. 3f), with the required band alignments to form a powerfully direct Z-scheme heterojunction for PHE application. The electron spin resonance (ESR) test is performed to corroborate more insight into the charge transfer mechanism. In Fig. S14, no DMPO-•O<sub>2</sub><sup>-</sup> peaks are observed over free-standing  $\alpha\text{-Fe}_2\text{O}_3$ , possibly due to its insufficient reduction potential to reduce O<sub>2</sub> to •O<sub>2</sub><sup>-</sup>. In contrast, it is visible for free NGr and binary  $\alpha\text{-Fe}_2\text{O}_3$  @NGr<sub>3</sub> samples. Noticeably, the binary entity shows strong DMPO-•O<sub>2</sub><sup>-</sup> peaks under light irradiation. Thus, the light-induced electrons can be concentrated in the conduction band of NGr via a direct Z-scheme heterojunction in the  $\alpha\text{-Fe}_2\text{O}_3$  @NGr<sub>3</sub> structure.

To examine charge carrier formation in as-prepared photocatalysts, LSV is performed in N<sub>2</sub>-saturated 0.1 M Na<sub>2</sub>SO<sub>4</sub> electrolyte with and without visible light irradiation at a sweep rate of 20 mV s<sup>-1</sup> from  $-0.3$ – $0.7$  V (vs. SCE). For this purpose, 5 mg of each photocatalyst is spray-deposited on the carbon cloth substrate (1 cm × 1 cm) with the microporous layer. In Fig. 4a, the free-standing  $\alpha\text{-Fe}_2\text{O}_3$  species as the photoanode generates no photocurrent in the dark, but its performance improves when exposed to visible light (0.25 mA cm<sup>-2</sup> at 0.7 V). Under the light, free NGr has a lower activity (0.16 mA cm<sup>-2</sup> at 0.7 V) than  $\alpha\text{-Fe}_2\text{O}_3$ . The performances of binary 2D/2D  $\alpha\text{-Fe}_2\text{O}_3$ -related Z-scheme heterostructures are improved after surface coating with NGr shells

compared to their parent materials. At 0.7 V, the photocurrent achieved is 0.32 mA cm<sup>-2</sup> for  $\alpha\text{-Fe}_2\text{O}_3$  @NGr<sub>1</sub>, 0.65 mA cm<sup>-2</sup> for  $\alpha\text{-Fe}_2\text{O}_3$  @NGr<sub>3</sub>, and 0.42 mA cm<sup>-2</sup> for  $\alpha\text{-Fe}_2\text{O}_3$  @NGr<sub>7</sub> (Fig. 4a and S15). Thus, encapsulating  $\alpha\text{-Fe}_2\text{O}_3$  with NGr shells on the surface can improve light absorption and charge generation in binary photocatalysts. However, the 7-nm-NGr-shell binary entity produces less charge than the 3-nm-shell binary entity, presumably due to its larger NGr shell thickness, which hinders light propagation to the interiors [5], limiting charge generation in the entire binary system. In the as-prepared samples, the three-factored 2D/2D  $\alpha\text{-Fe}_2\text{O}_3$  @NGr<sub>3</sub>-Pt<sub>SAs</sub> Z-scheme system under the same testing conditions achieves the maximum photocurrent density of 0.82 mA cm<sup>-2</sup>, which is 1.30-, 3.28-, and 5.13-fold greater than that of binary  $\alpha\text{-Fe}_2\text{O}_3$  @NGr<sub>3</sub>, free  $\alpha\text{-Fe}_2\text{O}_3$ , and NGr species. We also performed transient photocurrent response measurement (I-t curve) for the photocatalysts recorded in N<sub>2</sub>-saturated 0.1 M Na<sub>2</sub>SO<sub>4</sub> electrolyte with visible light irradiation, as shown in Fig. S16. The hybrid systems produced a higher photocurrent response than their parents, matching the previous LSV results. In addition, the EIS measurement was carried out to investigate the mobility of the light-induced charge carrier in the photocatalysts. As can be seen, the surface-functionalization with a thin Gr shell over  $\alpha\text{-Fe}_2\text{O}_3$  could enhance the light absorption and promote the photogenerated charge transfer into the hybridized photocatalysts (Fig. S17), particularly for the  $\alpha\text{-Fe}_2\text{O}_3$  @NGr<sub>3</sub>-Pt<sub>SAs</sub>, confirming the importance of the three-component catalyst. However, the separation efficiency of the photogenerated charge carrier is also considered (Fig. 4b and S18). A strong PL emission at about 510 nm was recorded for the NGr, while free-standing  $\alpha\text{-Fe}_2\text{O}_3$  displayed a broad PL peak emission up to 600 nm. Possibly due to the coating of the NGr shell on the surface of the  $\alpha\text{-Fe}_2\text{O}_3$  core, the PL signals of binary and ternary entities are mainly attributed to the single NGr component. Noticeably, the substantial PL quenching property over  $\alpha\text{-Fe}_2\text{O}_3$  @NGr<sub>3</sub> and  $\alpha\text{-Fe}_2\text{O}_3$

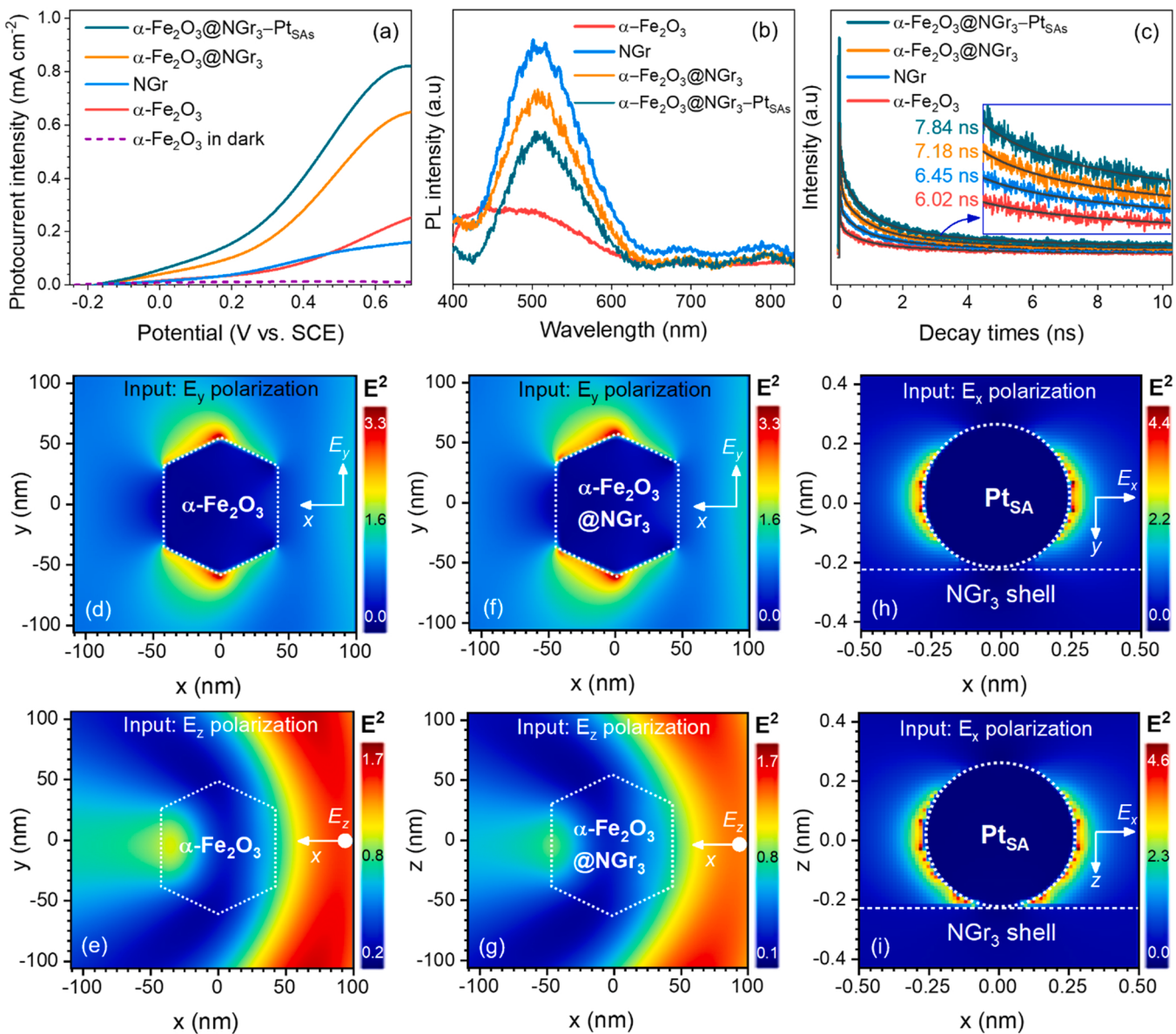


**Fig. 4.** (a) LSV polarization curves recorded at a sweep rate of  $20 \text{ mV s}^{-1}$  from  $-0.2$ – $0.7 \text{ V}$  (vs. SCE) in a  $\text{N}_2$ -saturated  $0.1 \text{ M Na}_2\text{SO}_4$  electrolyte in dark (dotted line) and under visible-light (solid line), (b and c) PL and TRPL spectra measured with an excitation wavelength of  $374 \text{ nm}$  and pulse width =  $1.0 \text{ ps}$  for as-prepared free-standing  $\alpha\text{-Fe}_2\text{O}_3$  and NGr species,  $\alpha\text{-Fe}_2\text{O}_3$  @NGr<sub>3</sub>, and  $\alpha\text{-Fe}_2\text{O}_3$  @NGr<sub>3</sub>-Pt<sub>SA</sub>. (d–i)  $E^2$  intensity profiles under different input polarizations for free-standing  $\alpha\text{-Fe}_2\text{O}_3$ , binary  $\alpha\text{-Fe}_2\text{O}_3$  @NGr<sub>3</sub>, and ternary  $\alpha\text{-Fe}_2\text{O}_3$  @NGr<sub>3</sub>-Pt<sub>SA</sub> simulated by FDTD method. (d)  $E_y$  and (e)  $E_z$  input polarization for  $\alpha\text{-Fe}_2\text{O}_3$ , (f)  $E_y$  and (g)  $E_z$  input polarization for  $\alpha\text{-Fe}_2\text{O}_3$  @NGr<sub>3</sub>. (h) xy-cut view and (i) xz-cut view of  $E^2$  intensity profiles under  $E_x$  input polarization for  $\alpha\text{-Fe}_2\text{O}_3$  @NGr<sub>3</sub>-Pt<sub>SA</sub>. The wavelength of the incident light is fixed at about  $503 \text{ nm}$ , and all the structures are surrounded by water with a refractive index of  $1.33$ .

@NGr<sub>3</sub>-Pt<sub>SA</sub> compared to free NGr (their lower PL intensities) indicates their restricted charge carrier recombination, resulting from the formation of a direct Z-scheme heterojunction. Furthermore, using an excitation wavelength of  $374 \text{ nm}$ , TRPL spectroscopy analyzes the decay periods of photogenerated charge carriers. The three-factored  $\alpha\text{-Fe}_2\text{O}_3$  @NGr<sub>3</sub>-Pt<sub>SA</sub> Z-scheme has the longest decay time of  $7.84 \text{ ns}$  in Fig. 4c, followed by the binary  $\alpha\text{-Fe}_2\text{O}_3$  @NGr<sub>3</sub> Z-scheme system ( $7.18 \text{ ns}$ ), free NGr ( $6.45 \text{ ns}$ ), and free  $\alpha\text{-Fe}_2\text{O}_3$  ( $6.02 \text{ ns}$ ). The TRPL results further support the initial PL analysis. Thus, the 2D/2D Z-scheme core-shell construction of  $\alpha\text{-Fe}_2\text{O}_3$  and NGr species can dramatically improve charge generation, separation, and transfer in the entire system, hugely beneficial for enhancing their photocatalytic properties.

Furthermore, the TFSF FDTD simulation was performed to calculate the distribution of electric intensity near the photocatalyst surface of various systems for better understanding. Fig. S19 shows the schematic views of the simulation based on the TEM images (Supplementary

Material). In the  $E_y$  input polarization, the electric field is substantially localized in the upper and lower corners of free 2D hexagonal  $\alpha\text{-Fe}_2\text{O}_3$  and binary 2D/2D  $\alpha\text{-Fe}_2\text{O}_3$  @NGr<sub>3</sub> species (see Figs. 4d and f). Furthermore, the field profiles in Figs. 4e and g show that the incident light is highly dispersed at the surface of these two systems, likely improving the light absorption by 2D-contained structures. According to the FDTD-calculated absorption cross-section results, the  $\alpha\text{-Fe}_2\text{O}_3$  @NGr<sub>3</sub> heterojunction has a higher light absorption capability (e.g., on  $E_y$  polarization) than free-standing  $\alpha\text{-Fe}_2\text{O}_3$  (Fig. S20), which is consistent with the previously examined UV-vis DRS data. It may result in a greater electric field intensity being generated on the binary system's surface. The electric field generated in  $\alpha\text{-Fe}_2\text{O}_3$  @NGr<sub>3</sub> would be localized to the third component, such as the Pt cocatalyst. The field is greatly amplified on the surface of the Pt single-atom with the radius of  $0.25 \text{ nm}$  in the ternary system, as seen in Fig. 4h and i, indicating that electrons have been collected in this region. Notably, on the xz-plane, the electric

field is localized around the interface between the NGr and Pt species, known as hotspots, increasing the potential for PHE utilization of the three-factored direct 2D/2D Z-scheme-based  $\alpha\text{-Fe}_2\text{O}_3$  @NGr<sub>3</sub>–Pt<sub>SAs</sub> system.

### 3.2. PHE performances and mechanisms

Practical PHE evaluations of the as-prepared photocatalysts were carried out in a mixed aqueous sacrificial agent, including 0.25 M Na<sub>2</sub>SO<sub>3</sub> and 0.25 M Na<sub>2</sub>S, which functioned as efficient hole scavengers with the help of visible light irradiation ( $\lambda > 420$  nm). The free-standing  $\alpha\text{-Fe}_2\text{O}_3$  with a positive CBM value and Gr entities typically exhibit no PHE activity, as demonstrated in Fig. 5a and S21 (Supplementary Material). Therefore, we did not extendedly consider depositing the Pt-containing cocatalysts on these inactive support materials. The NGr candidate outperforms the others. The binary systems ( $\alpha\text{-Fe}_2\text{O}_3$  @Gr and NGr–Pt<sub>SAs</sub>) outperform their constituents in terms of PHE activity. Over a 4-h testing cycle, the three-factored 2D/2D Z-scheme systems ( $\alpha\text{-Fe}_2\text{O}_3$  @NGr<sub>3</sub>–Pt<sub>SAs</sub> and  $\alpha\text{-Fe}_2\text{O}_3$  @NGr<sub>3</sub>–Pt<sub>NPs</sub>) exhibit the greatest evolved hydrogen levels, reaching up to 25.6 and 21.0  $\mu\text{mol mg}_{\text{cat}}^{-1}\text{ h}^{-1}$ . Fig. 5a shows that the relevant PHE rate for the ternary  $\alpha\text{-Fe}_2\text{O}_3$  @NGr<sub>3</sub>–Pt<sub>SAs</sub> photocatalyst is approximately 6.4  $\mu\text{mol mg}_{\text{cat}}^{-1}\text{ h}^{-1}$ , which is 16.4-, 5.16-, 3.28-, 4.21-, and 3.56-times higher than those of free NGr (0.39  $\mu\text{mol mg}_{\text{cat}}^{-1}\text{ h}^{-1}$ ),  $\alpha\text{-Fe}_2\text{O}_3$  @NGr<sub>1</sub> (1.24  $\mu\text{mol mg}_{\text{cat}}^{-1}\text{ h}^{-1}$ ),  $\alpha\text{-Fe}_2\text{O}_3$  @NGr<sub>3</sub> (1.95  $\mu\text{mol mg}_{\text{cat}}^{-1}\text{ h}^{-1}$ ),  $\alpha\text{-Fe}_2\text{O}_3$  @NGr<sub>7</sub> (1.52  $\mu\text{mol mg}_{\text{cat}}^{-1}\text{ h}^{-1}$ ), and NGr–Pt<sub>SAs</sub> (1.80  $\mu\text{mol mg}_{\text{cat}}^{-1}\text{ h}^{-1}$ ) species, respectively. Even though it has a lower Pt cocatalyst loading (0.5 wt%) than Pt NPs-related species (2.0 wt%), the performance of  $\alpha\text{-Fe}_2\text{O}_3$  @NGr<sub>3</sub>–Pt<sub>SAs</sub> is 1.22-times larger than that of  $\alpha\text{-Fe}_2\text{O}_3$  @NGr<sub>3</sub>–Pt<sub>NPs</sub> (5.25  $\mu\text{mol mg}_{\text{cat}}^{-1}\text{ h}^{-1}$ ). Reducing Pt cocatalysts to

single-atom species significantly improves PHE performance for the three-factored 2D/2D  $\alpha\text{-Fe}_2\text{O}_3$  @NGr<sub>3</sub>–Pt<sub>SAs</sub> Z-scheme system. PHE durability is also assessed over NGr,  $\alpha\text{-Fe}_2\text{O}_3$  @NGr<sub>3</sub>, and  $\alpha\text{-Fe}_2\text{O}_3$  @NGr<sub>3</sub>–Pt<sub>SAs</sub> species for five repeating cycles within 20 h. In Fig. 5b, the three-factored photocatalyst system loses just 7.0% of its activity after five repetitions compared to the initial cycle, but the  $\alpha\text{-Fe}_2\text{O}_3$  @NGr<sub>3</sub> and NGr photocatalysts lose 21.0% and 46.0%, respectively. After a 20-h visible light irradiation run, the ternary  $\alpha\text{-Fe}_2\text{O}_3$  @NGr<sub>3</sub>–Pt<sub>SAs</sub> Z-scheme fabrication demonstrates a durable PHE system. After the durability test, the as-exposed  $\alpha\text{-Fe}_2\text{O}_3$  @NGr<sub>3</sub>–Pt<sub>SAs</sub> sample is re-characterized by XRD and SEM. In Fig. S22a, the XRD analysis demonstrates no change in the crystalline phase of the as-exposed  $\alpha\text{-Fe}_2\text{O}_3$  @NGr<sub>3</sub>–Pt<sub>SAs</sub> entity. Furthermore, the relevant morphology and structure are well-preserved for the ternary Z-scheme system after long-time exposure to PHE reactions via FESEM observation (Fig. S22b), validating the excellent structural stability of the photocatalyst for long-term PHE utilization. Under visible light irradiation, the enhanced PHE performance of three-factored direct 2D/2D  $\alpha\text{-Fe}_2\text{O}_3$  @NGr<sub>3</sub>–Pt<sub>SAs</sub> Z-scheme construction is comparable to that of reportedly available photocatalysts, as shown in Fig. 5c. As a result, the ternary  $\alpha\text{-Fe}_2\text{O}_3$  @NGr<sub>3</sub>–Pt<sub>SAs</sub> discovered in this study outperforms the presently single-, binary-, ternary-, and direct Z-scheme-based systems in terms of PHE [19,37–54]. On the other hand, the hydrogen evolution over the ternary  $\alpha\text{-Fe}_2\text{O}_3$  @NGr<sub>3</sub>–Pt<sub>SAs</sub> entity is further evaluated under actual sunlight irradiation. As shown in Fig. S23, the PHE performance under sunlight (6.7  $\mu\text{mol mg}_{\text{cat}}^{-1}\text{ h}^{-1}$ ) is higher (~4.7%) than that obtained under visible irradiation. The negligible increase can be assigned to the presence of a small portion of the ultraviolet source (below 4%) in the sunlight irradiation, which can support the generation of more electron-hole pairs in the Z-scheme

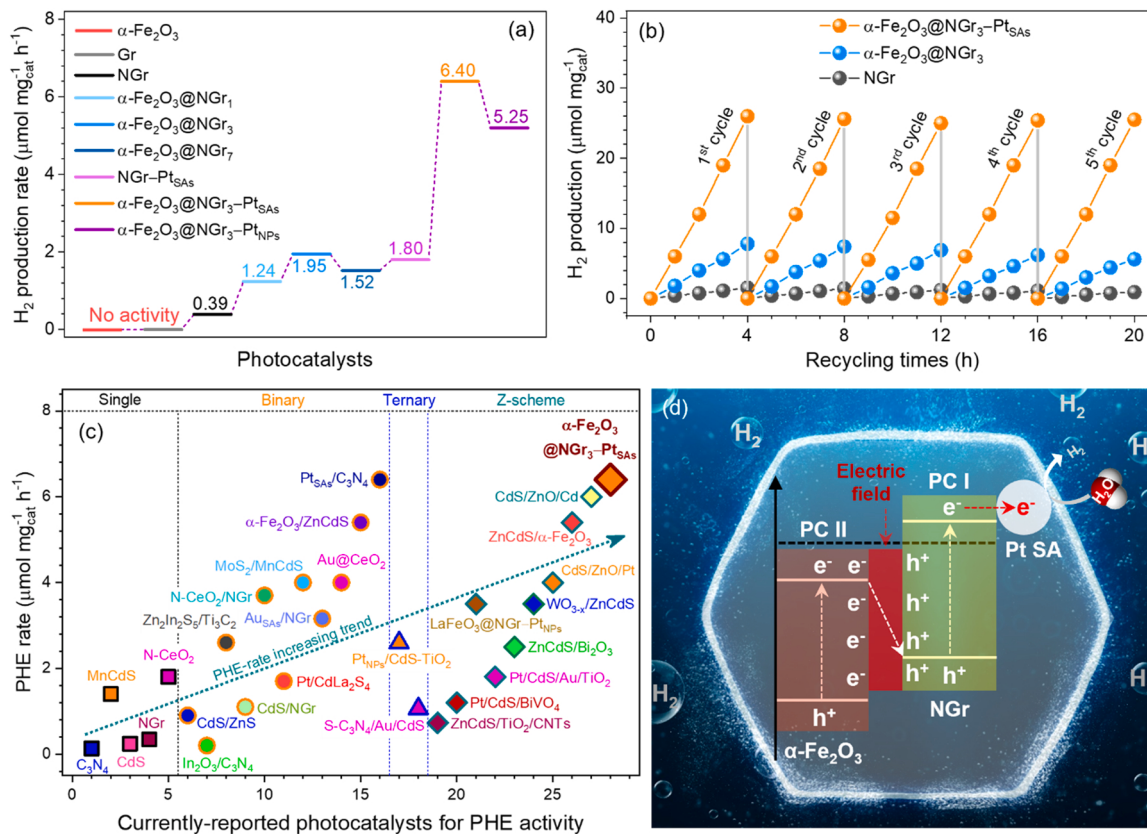
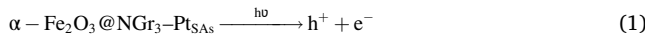


**Fig. 5.** Practical PHE evaluation in a mixed aqueous solution of 0.25 M Na<sub>2</sub>SO<sub>3</sub> and 0.25 M Na<sub>2</sub>S electrolyte under visible-light irradiation: (a) PHE rate for all as-prepared photocatalysts and (b) PHE durability activity over five sequential cycles (20 h in total) for  $\alpha\text{-Fe}_2\text{O}_3$ ,  $\alpha\text{-Fe}_2\text{O}_3$  @NGr<sub>3</sub>, and  $\alpha\text{-Fe}_2\text{O}_3$  @NGr<sub>3</sub>–Pt<sub>SAs</sub>. (c) The visible light-driven PHE rates are compared to the currently available single, binary, ternary, and Z-scheme photocatalysts. (d) Possible mechanism generation and transfer of electron–hole pairs into ternary  $\alpha\text{-Fe}_2\text{O}_3$  @NGr<sub>3</sub>–Pt<sub>SAs</sub> heterojunction photocatalyst for promoting hydrogen evolution reactions based on a direct Z-scheme system under visible-light irradiation.

system.

This work proposes an advanced feasible PHE mechanism over the ternary direct 2D/2D  $\alpha$ -Fe<sub>2</sub>O<sub>3</sub> @NGr<sub>3</sub>-Pt<sub>SAs</sub> Z-scheme system. To begin, it should be observed that free-standing hexagonal  $\alpha$ -Fe<sub>2</sub>O<sub>3</sub> with a positive CB potential (+0.36 V vs. NHE) and Gr species exhibit no PHE activity when exposed to visible light. Once the N atoms are doped into the Gr host, the Fermi position in the NGr is shifted to the VB position, resulting in an n-type semiconductor. The resulting NGr with a bandgap energy of (2.11 eV, Fig. 3f) may absorb low-energy photons in the visible light region and generate the electron-hole pairs. As a result of reaching a hydrogen reduction potential, the 2D NGr can produce a determinable volume of hydrogen (~0.45 V vs. NHE, Fig. 3c). Incorporating Pt SAs on the NGr host can also improve their PHE target. Because of its low potential, the Pt SAs cocatalyst acts as an electron scavenger [55], causing light-induced electrons in the NGr photocatalyst to migrate to the cocatalyst surface and speed up proton reduction to H<sub>2</sub> gas. The direct 2D/2D  $\alpha$ -Fe<sub>2</sub>O<sub>3</sub> @NGr<sub>3</sub> Z-scheme system, in which the  $\alpha$ -Fe<sub>2</sub>O<sub>3</sub> acts as the PC II system and the NGr as the PC I system, demonstrates increased hydrogen production. Indeed, electron-hole pairs are separately produced in the  $\alpha$ -Fe<sub>2</sub>O<sub>3</sub> and NGr photocatalysts using visible light. The light-induced weaker reducing electrons in the CB of  $\alpha$ -Fe<sub>2</sub>O<sub>3</sub> will then be captured by the weaker oxidizing holes in the VB of NGr due to interfacial interactions, as shown in Fig. 5d. In the binary catalyst, electrons and holes with higher redox potentials are concurrently accumulated at the CB of NGr and the VB of  $\alpha$ -Fe<sub>2</sub>O<sub>3</sub>. As a result, the direct 2D/2D Z-scheme design with the presence of Fe-N bond is considerably beneficial for charge generation and separation under light illumination, resulting in improved PHE. Furthermore, implantation of a Pt cocatalyst on the surface of a binary system can increase photoconversion. In the three-factored 2D/2D  $\alpha$ -Fe<sub>2</sub>O<sub>3</sub> @NGr<sub>3</sub>-Pt<sub>SAs</sub> Z-scheme system, the light-excited electrons in the CB level of NGr are transported to the Pt cocatalyst to accomplish the hydrogen generation process, while the holes in the VB of  $\alpha$ -Fe<sub>2</sub>O<sub>3</sub> are trapped by the S<sup>2-</sup> and SO<sub>3</sub><sup>2-</sup> sacrificial agents. On the one hand, adding a sacrificial agent can increasingly capture the Z-shaped hole in the valence band of  $\alpha$ -Fe<sub>2</sub>O<sub>3</sub> PC II under light irradiation due to its higher molecule polarity and more substantial oxidation potential than water. On the other hand, the light-induced holes can convert Na<sub>2</sub>SO<sub>3</sub>/Na<sub>2</sub>S to SO<sub>4</sub><sup>2-</sup>/S<sub>2</sub><sup>2-</sup>, preventing the generation of oxygen gas from the water in the reaction chamber. Subsequently, high-purity hydrogen gas can solely be obtained in the presence of Na<sub>2</sub>SO<sub>3</sub> and Na<sub>2</sub>S hole scavengers. Thus, under visible light irradiation, the entire redox catalytic reactions over the direct Z-scheme system are formulated as follows:

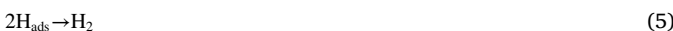
a) Electron-hole pairs separation:



b) Oxidation of sacrificial agents (Na<sub>2</sub>SO<sub>3</sub> + Na<sub>2</sub>S) at the VB of  $\alpha$ -Fe<sub>2</sub>O<sub>3</sub>:



c) Proton reduction to H<sub>2</sub> gas at the surface of Pt cocatalysts:



The Pt SAs-contained entity outperforms the Pt NPs-contained entity in the ternary Z-scheme systems studied, attributed to the two following effects. (i) As seen in TEM images (Fig. 1f), the Pt SAs are uniformly distributed on the surface of the NGr shell, expanding the interfacial interactions between the PC I and the cocatalyst species and facilitating

light-produced charge transfer. (ii) In comparison to the Pt NPs-related design, the Pt SAs-related design has free adsorption energy of hydrogen atoms on the Pt SAs close to zero (0 eV, where optimal catalysts can be fabricated), as confirmed by the density functional theory (DFT) calculations below.

### 3.3. DFT calculations of the PHE activity

The properties of the catalysts described in the previous Sections have been investigated by means of DFT calculations as implemented in the VASP code and adopting PBE+U exchange correlation functional. Hydrogen adsorption and evolution have been studied for the same catalysts investigated experimentally.  $\alpha$ -Fe<sub>2</sub>O<sub>3</sub> has been simulated by considering the hydroxylated (0001) surface since this is the common termination found in an aqueous environment [56]; NGr has been modeled by a graphene monolayer where 4% of N atoms are incorporated in the structure. With these two components, we have constructed the  $\alpha$ -Fe<sub>2</sub>O<sub>3</sub> @NGr heterojunction with the side and top views, and the density of states of the optimized interface are shown in Fig. 6(a-c). When modeling an interface, the main problem is the generation of a working unit cell where the mismatch is minimized [57]. This can be achieved by adopting a 2 × 2 supercell of  $\alpha$ -Fe<sub>2</sub>O<sub>3</sub> and 4 × 4 supercell of NGr, resulting in an acceptable mismatch of 2.0%, 2.0%, and 0% for *a*, *b* and *g* lattice parameters. We fixed the lattice parameters to those of the  $\alpha$ -Fe<sub>2</sub>O<sub>3</sub> support, deposited a single NGr layer, and optimized all the atomic coordinates. The bond lengths between Fe-C, Fe-N, C-N, and Fe-O are reported. The adhesion energy, 0.20 J m<sup>-2</sup>, is typical of Van der Waals interfaces, which indicates that the formation of the interface is thermodynamically favorable (for further details, see Supplementary Material) [58]. The analysis of the interface dipole and charge density difference indicates an electron accumulation on the  $\alpha$ -Fe<sub>2</sub>O<sub>3</sub> side of the interface and consequent depletion of charge density at NGr side (Fig. 6d). This is rationalizable in terms of a direct Z-scheme behavior of the  $\alpha$ -Fe<sub>2</sub>O<sub>3</sub>/NGr interface, which is at the basis of the observed photoactivity (Fig. 3f).

Pt atoms have been deposited on a bridge site (most favorable) of NGr and  $\alpha$ -Fe<sub>2</sub>O<sub>3</sub> @NGr, resulting in NGr-Pt<sub>SAs</sub> and  $\alpha$ -Fe<sub>2</sub>O<sub>3</sub> @NGr-Pt<sub>SAs</sub> model catalysts while representing Pt NPs, due to their dimensions, we used an extended Pt(111) surface (see Fig. S24-31). A H atom has been adsorbed on these catalysts, and the free energy of adsorption,  $\Delta G_H$ , has been computed. According to a widely adopted model proposed by Nørskov in 2005 [59], a good catalyst for hydrogen evolution is characterized by a small  $\Delta G_H$  as this corresponds to a catalyst that binds neither too strongly nor too weakly the H atom. A catalyst with  $\Delta G_H = 0$  would be ideal, as this corresponds to the top of the volcano plot according to the Sabatier principle. With this simple model, which neglects various aspects of the reaction, such as the possible formation of other intermediates or the effect of the solvent [23,60], one can obtain an initial estimate of the activity of a catalyst in HER.

Fig. 6e reports the computed free energies for H adsorption on the various catalyst considered (see also Supplementary Material). NGr is not particularly active since it has a  $\Delta G_H$  of 0.65 eV, indicating low H binding capability; this is consistent with the experimental observation as this is the weakest catalyst among those considered here. On the other extreme is NGr-Pt<sub>SAs</sub> since the Pt atom binds H too strongly ( $\Delta G_H = -0.84$ ). Also, the  $\alpha$ -Fe<sub>2</sub>O<sub>3</sub> surface, with  $\Delta G_H = -0.79$  eV, is a poor catalyst due to a strong affinity for H (Fig. 6e). The situation improves if NGr and  $\alpha$ -Fe<sub>2</sub>O<sub>3</sub> are combined to form an interface:  $\alpha$ -Fe<sub>2</sub>O<sub>3</sub> @NGr exhibits a  $\Delta G_H = 0.46$  eV, with a clear improvement with respect to the separated units. The higher activity of Fe<sub>2</sub>O<sub>3</sub> @NGr compared to NGr is in line with the observations. The hydrogen evolution activity is further improved if a Pt atom is added to  $\alpha$ -Fe<sub>2</sub>O<sub>3</sub> @NGr to form  $\alpha$ -Fe<sub>2</sub>O<sub>3</sub> @NGr-Pt<sub>SAs</sub>. With this catalyst  $\Delta G_H$  becomes -0.26 eV, sufficiently small in absolute value to suggest a high activity. Interestingly, a Pt(111) surface, representing Pt NPs, binds hydrogen with a  $\Delta G_H$  equal in absolute value but opposite in sign, 0.26 eV (Fig. 6e). According to the Nørskov model,

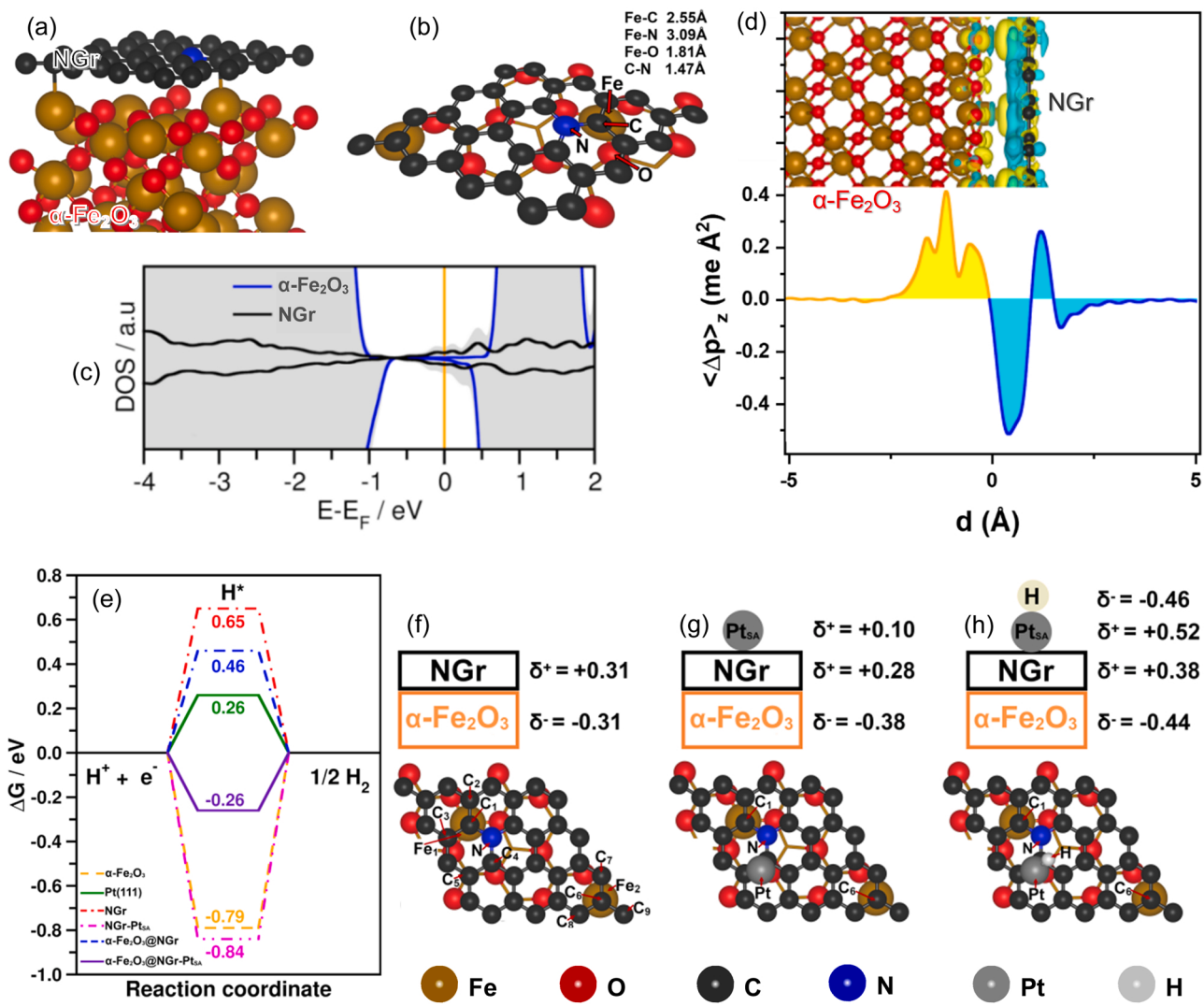


**Fig. 6.** (a) Side and (b) top views, (c) density of states of the optimized  $\alpha\text{-Fe}_2\text{O}_3$  @NGr heterojunction, (d) plane-averaged charge density difference plot  $<\Delta\rho>_z$  of the  $\alpha\text{-Fe}_2\text{O}_3$  @NGr interface, orange and blue lines are for  $\alpha\text{-Fe}_2\text{O}_3$  and NGr units. Charge density accumulation and depletion regions are reported in yellow and light blue respectively. (e) H adsorption free energy on the various catalysts considered in this work; charge polarization at the interface of (f)  $\alpha\text{-Fe}_2\text{O}_3$  @NGr, (g)  $\alpha\text{-Fe}_2\text{O}_3$  @NGr—Pt<sub>SA</sub>, and (h)  $\alpha\text{-Fe}_2\text{O}_3$  @NGr—Pt<sub>SA</sub>—H species.

this suggests that  $\alpha\text{-Fe}_2\text{O}_3$  @NGr-Pt<sub>SA</sub> and Pt NPs should have comparable activities. In the experiment,  $\alpha\text{-Fe}_2\text{O}_3$  @NGr-Pt<sub>SA</sub> is about 20% more active than Pt NPs a result that, considering the various approximations inherent to the models used, can be considered as fully consistent. Thus, the order of activity in hydrogen evolution according to the DFT calculations is  $\alpha\text{-Fe}_2\text{O}_3$  @NGr-Pt<sub>SA</sub> >  $\alpha\text{-Fe}_2\text{O}_3$  @NGr > NGr, the same order found experimentally.

The last question to address is why by combining NGr with  $\alpha\text{-Fe}_2\text{O}_3$  the activity in hydrogen evolution is enhanced. Fig. 6f shows that a substantial charge polarization is present at the  $\alpha\text{-Fe}_2\text{O}_3$  @NGr interface with positive charge that accumulates on NGr and negative charge on  $\alpha\text{-Fe}_2\text{O}_3$ . This is further corroborated by the analysis of the charge density difference (see Fig. 6d). Furthermore, the charge polarization at the interface is also present after Pt deposition (Fig. 6g). This charge polarization results in the modified activity of the supported Pt atom and in more suitable H binding capability, as shown in Fig. 6h. In fact, going from the unsupported NGr-Pt<sub>SA</sub> catalyst to  $\alpha\text{-Fe}_2\text{O}_3$  @NGr-Pt<sub>SA</sub>, the free energy of H adsorption changes from  $-0.84$  eV to  $-0.26$  eV, which corresponds to going from a modest to a good catalyst.

#### 4. Conclusion

An efficient and durable direct Z-scheme photocatalyst for visible-light-to-hydrogen conversion is synthesized using a ternary 2D/2D  $\alpha\text{-Fe}_2\text{O}_3$  @NGr<sub>3</sub>-Pt<sub>SA</sub>s core-shell structure (NGr shell thickness of 3 nm and Pt loading of 0.5 wt%). The discovered ternary direct Z-scheme has a better PHE performance under visible light irradiation, reaching up to  $6.4 \mu\text{mol mg}_{\text{cat}}^{-1} \text{ h}^{-1}$ , which is 16.4-, 3.28-, and 1.22-times greater than those of NGr ( $0.39 \mu\text{mol mg}_{\text{cat}}^{-1} \text{ h}^{-1}$ ) and  $\alpha\text{-Fe}_2\text{O}_3$  @NGr<sub>3</sub> ( $1.95 \mu\text{mol mg}_{\text{cat}}^{-1} \text{ h}^{-1}$ ), and ternary Pt nanoparticles-containing catalyst ( $5.25 \mu\text{mol mg}_{\text{cat}}^{-1} \text{ h}^{-1}$ , with Pt loading of 2.0 wt%), respectively. This achievement outperforms previously reported PHE catalysts under visible light irradiation. The following are the implicit explanations for these outstanding achievements over the ternary catalyst studied. (1) Under visible light irradiation, the suitable interfacial interactions between  $\alpha\text{-Fe}_2\text{O}_3$  and NGr facilitate charge separation and transfer. (2) The enhanced direct Z-scheme design generates many active charge carriers for PHE reactions. (3) Finally, the Pt SAs attached to the NGr host's surface attract Z-scheme electrons, accelerating proton reduction to hydrogen. This discovery paves the way for converting visible light-to-fuels using the three-factored direct 2D/2D Z-scheme core-shell construction.

## CRediT authorship contribution statement

**Vandung Dao:** Conceptualization, Methodology, Software, Formal Analysis, Investigation, Resources, Data Curation, Writing – Original Draft, **Luis A. Cipriano:** Methodology, Software, Formal Analysis, Resources, Data Curation, Writing – Original Draft, **Sang-Woo Ki:** Software and Formal Analysis, **Sunny Yadav:** Data Curation and Analysis, **Wenmeng Wang:** Morphological Analysis, **Giovanni Di Liberto:** Formal Analysis, Resources, Data Curation, **Kai Chen:** Resources, Data Curation, **Hoki Son:** Software, Formal Analysis, **Jin-Kyu Yang:** Visualization, Supervision, Project Administration, Funding Acquisition, **Gianfranco Pacchioni:** Visualization, Supervision, Project Administration, Funding Acquisition, **In-Hwan Lee:** Writing – Review & Editing, Visualization, Supervision, Project Administration, Funding Acquisition.

## Declaration of Competing Interest

The authors declare that they have no known competing financial interests or personal relationships that could have appeared to influence the work reported in this paper.

## Data Availability

No data was used for the research described in the article.

## Acknowledgments

This work was supported by the National Research Foundation of Korea (NRF) grant funded by the Korea government (MSIT) (2021M3H4A1A02051284, 2022R1A2C1010895, 2020R1A2C1014498), and the Industrial Strategic Technology Development Program (20019235, Deformable and Immersive Volumetric AR Glass) funded by the Ministry of Trade, Industry & Energy (MOTIE, Korea). LAC, GDL, and GP acknowledge the financial support from the Italian Ministry of University and Research (MUR) through the PRIN Project 20179337R7 and the access to the CINECA supercomputing resources via ISCRAE.

## Appendix A. Supporting information

Supplementary data associated with this article can be found in the online version at [doi:10.1016/j.apcatb.2023.122586](https://doi.org/10.1016/j.apcatb.2023.122586).

## References

- [1] J. Lee, C. Yeon, J. Oh, G. Han, J. Do Yoo, H.J. Yun, C.-W. Lee, K.T. Lee, J. Bae, Highly active and stable catalyst with exsolved PtRu alloy nanoparticles for hydrogen production via commercial diesel reforming, *Appl. Catal. B: Environ.* 316 (2022), 121645.
- [2] Z. Shao, S. Zhang, X. Liu, H. Luo, C. Huang, H. Zhou, Z. Wu, J. Li, H. Wang, Y. Sun, Maximizing the synergistic effect between Pt<sup>0</sup> and Pt<sup>δ+</sup> in a confined Pt-based catalyst for durable hydrogen production, *Appl. Catal. B: Environ.* 316 (2022), 121669.
- [3] D. Kim, K. Yong, Boron doping induced charge transfer switching of a C<sub>3</sub>N<sub>4</sub>/ZnO photocatalyst from Z-scheme to type II to enhance photocatalytic hydrogen production, *Appl. Catal. B: Environ.* 282 (2021), 119538.
- [4] J. Oh, J.M. Lee, Y. Yoo, J. Kim, S.-J. Hwang, S. Park, New insight of the photocatalytic behaviors of graphitic carbon nitrides for hydrogen evolution and their associations with grain size, porosity, and photophysical properties, *Appl. Catal. B: Environ.* 218 (2017) 349–358.
- [5] D. Van Dao, H. Choi, T.T.D. Nguyen, S.-W. Ki, G.-C. Kim, H. Son, J.-K. Yang, Y.-T. Yu, H.Y. Kim, I.-H. Lee, Light-to-hydrogen improvement based on three-factored Au@CeO<sub>2</sub>/Gr hierarchical photocatalysts, *ACS Nano* 16 (2022) 7848–7860.
- [6] Y. Kim, D. Shin, W.J. Chang, H.L. Jang, C.W. Lee, H.-E. Lee, K.T. Nam, Hybrid Z-scheme using photosystem I and BiVO<sub>4</sub> for hydrogen production, *Adv. Funct. Mater.* 25 (2015) 2369–2377.
- [7] Y. Geng, D. Chen, N. Li, Q. Xu, H. Li, J. He, J. Lu, Z-Scheme 2D/2D α-Fe<sub>2</sub>O<sub>3</sub>/g-C<sub>3</sub>N<sub>4</sub> heterojunction for photocatalytic oxidation of nitric oxide, *Appl. Catal. B: Environ.* 280 (2021), 119409.
- [8] D. Van Dao, G. Di Liberto, H. Ko, J. Park, W. Wang, D. Shin, H. Son, Q. Van Le, T. Van Nguyen, V. Van Tan, G. Pacchioni, I.-H. Lee, LaFeO<sub>3</sub> meets nitrogen-doped graphene functionalized with ultralow Pt loading in an impactful Z-scheme platform for photocatalytic hydrogen evolution, *J. Mater. Chem. A* 10 (2022) 3330–3340.
- [9] X. Ma, G. Wang, L. Qin, J. Liu, B. Li, Y. Hu, H. Cheng, Z-scheme g-C<sub>3</sub>N<sub>4</sub>-AQ-MoO<sub>3</sub> photocatalyst with unique electron transfer channel and large reduction area for enhanced sunlight photocatalytic hydrogen production, *Appl. Catal. B: Environ.* 288 (2021), 120025.
- [10] Y. Wu, H. Wang, W. Tu, Y. Liu, S. Wu, Y.Z. Tan, J.W. Chew, Construction of hierarchical 2D–2D Zn<sub>3</sub>In<sub>2</sub>S<sub>6</sub>/fluorinated polymeric carbon nitride nanosheets photocatalyst for boosting photocatalytic degradation and hydrogen production performance, *Appl. Catal. B: Environ.* 233 (2018) 58–69.
- [11] H.J. Choi, M. Dincă, A. Dailly, J.R. Long, Hydrogen storage in water-stable metal–organic frameworks incorporating 1,3- and 1,4-benzenedipyrizolate, *Energy Environ. Sci.* 3 (2010) 117–123.
- [12] A. Helal, F.A. Harraz, A.A. Ismail, T.M. Sami, I.A. Ibrahim, Hydrothermal synthesis of novel heterostructured Fe<sub>2</sub>O<sub>3</sub>/Bi<sub>2</sub>S<sub>3</sub> nanorods with enhanced photocatalytic activity under visible light, *Appl. Catal. B: Environ.* 213 (2017) 18–27.
- [13] S. Shanavas, S. Mohana Roopan, A. Priyadharsan, D. Devipriya, S. Jayapandi, R. Acevedo, P.M. Anbarasan, Computationally guided synthesis of (2D/3D/2D) rGO/Fe<sub>2</sub>O<sub>3</sub>/g-C<sub>3</sub>N<sub>4</sub> nanostructure with improved charge separation and transportation efficiency for degradation of pharmaceutical molecules, *Appl. Catal. B: Environ.* 255 (2019), 117758.
- [14] J.-C. Wang, L. Zhang, W.-X. Fang, J. Ren, Y.-Y. Li, H.-C. Yao, J.-S. Wang, Z.-J. Li, Enhanced photoreduction CO<sub>2</sub> activity over direct Z-scheme α-Fe<sub>2</sub>O<sub>3</sub>/Cu<sub>2</sub>O heterostructures under visible light irradiation, *ACS Appl. Mater. Interfaces* 7 (2015) 8631–8639.
- [15] T. Tabari, M. Kobielszus, J. Duch, D. Singh, A. Kotarba, W. Maczik, Design, engineering, and performance of nanorod-Fe<sub>2</sub>O<sub>3</sub>@rGO@LaSrFe<sub>2-n</sub>Co<sub>n</sub>O<sub>6</sub> (n = 0, 1) composite architectures: the role of double oxide perovskites in reaching high solar to hydrogen efficiency, *Appl. Catal. B: Environ.* 272 (2020), 118952.
- [16] S. He, C. Yan, X.-Z. Chen, Z. Wang, T. Ouyang, M.-L. Guo, Z.-Q. Liu, Construction of core-shell heterojunction regulating α-Fe<sub>2</sub>O<sub>3</sub> layer on CeO<sub>2</sub> nanotube arrays enables highly efficient Z-scheme photoelectrocatalysis, *Appl. Catal. B: Environ.* 276 (2020), 119138.
- [17] S.-J. Jeon, T.-W. Kang, J.-M. Ju, M.-J. Kim, J.H. Park, F. Raza, J. Han, H.-R. Lee, J.-H. Kim, Modulating the photocatalytic activity of graphene quantum dots via atomic tailoring for highly enhanced photocatalysis under visible light, *Adv. Funct. Mater.* 26 (2016) 8211–8219.
- [18] K.M. Kamal, R. Narayan, N. Chandran, S. Popović, M.A. Nazrulla, J. Kovač, N. Vrtovec, M. Bele, N. Hodnik, M.M. Kržmanc, B. Likozar, Synergistic enhancement of photocatalytic CO<sub>2</sub> reduction by plasmonic Au nanoparticles on TiO<sub>2</sub> decorated N-graphene heterostructure catalyst for high selectivity methane production, *Appl. Catal. B: Environ.* 307 (2022), 121181.
- [19] D. Van Dao, L.A. Cipriano, G. Di Liberto, T.T.D. Nguyen, S.-W. Ki, H. Son, G.-C. Kim, K.H. Lee, J.-K. Yang, Y.-T. Yu, G. Pacchioni, I.-H. Lee, Plasmonic Au nanoclusters dispersed in nitrogen-doped graphene as a robust photocatalyst for light-to-hydrogen conversion, *J. Mater. Chem. A* 9 (2021) 22810–22819.
- [20] Q. Zhao, J. Sun, S. Li, C. Huang, W. Yao, W. Chen, T. Zeng, Q. Wu, Q. Xu, Single nickel atoms anchored on nitrogen-doped graphene as a highly active cocatalyst for photocatalytic H<sub>2</sub> evolution, *ACS Catal.* 8 (2018) 11863–11874.
- [21] F. Zhang, Y. Zhu, Q. Lin, L. Zhang, X. Zhang, H. Wang, Noble-metal single-atoms in thermocatalysis, electrocatalysis, and photocatalysis, *Energy Environ. Sci.* 14 (2021) 2954–3009.
- [22] A. Kumar, V.Q. Bui, J. Lee, L. Wang, A.R. Jadhav, X. Liu, X. Shao, Y. Liu, J. Yu, Y. Hwang, H.T.D. Bui, S. Ajmal, M.G. Kim, S.-G. Kim, G.-S. Park, Y. Kawazoe, H. Lee, Moving beyond bimetallic-alloy to single-atom dimer atomic-interface for all-pH hydrogen evolution, *Nat. Commun.* 12 (2021) 6766.
- [23] G. Di Liberto, L.A. Cipriano, G. Pacchioni, Role of dihydride and dihydrogen complexes in hydrogen evolution reaction on single-atom catalysts, *J. Am. Chem. Soc.* 143 (2021) 20431–20441.
- [24] H. Jeong, O. Kwon, B.-S. Kim, J. Bae, S. Shin, H.-E. Kim, J. Kim, H. Lee, Highly durable metal ensemble catalysts with full dispersion for automotive applications beyond single-atom catalysts, *Nat. Catal.* 3 (2020) 368–375.
- [25] X. Xiao, Y. Gao, L. Zhang, J. Zhang, Q. Zhang, Q. Li, H. Bao, J. Zhou, S. Miao, N. Chen, J. Wang, B. Jiang, C. Tian, H. Fu, A promoted charge separation/transfer system from Cu single atoms and C<sub>3</sub>N<sub>4</sub> layers for efficient photocatalysis, *Adv. Mater.* 32 (2020) 2003082.
- [26] D. Lee, Y. Kim, Y. Kwon, J. Lee, T.-W. Kim, Y. Noh, W.B. Kim, M.H. Seo, K. Kim, H. J. Kim, Boosting the electrocatalytic glycerol oxidation performance with highly-dispersed Pt nanoclusters loaded on 3D graphene-like microporous carbon, *Appl. Catal. B: Environ.* 245 (2019) 555–568.
- [27] M. Zhu, Y. Wang, D. Meng, X. Qin, G. Diao, Hydrothermal synthesis of hematite nanoparticles and their electrochemical properties, *J. Phys. Chem. C* 116 (2012) 16276–16285.
- [28] G. Kresse, J. Furthmüller, Efficient iterative schemes for ab initio total-energy calculations using a plane-wave basis set, *Phys. Rev. B* 54 (1996) 11169–11186.
- [29] G. Kresse, D. Joubert, From ultrasoft pseudopotentials to the projector augmented-wave method, *Phys. Rev. B* 59 (1999) 1758–1775.
- [30] J.P. Perdew, K. Burke, M.J.P. Ernzerhof, Generalized gradient approximation made simple, *Phys. Rev. Lett.* 77 (1996) 3865.
- [31] V.I. Anisimov, J. Zaanen, O.K. Andersen, Band theory and Mott insulators: Hubbard U instead of Stoner I, *Phys. Rev. B* 44 (1991) 943–954.
- [32] G. Rollmann, A. Rohrbach, P. Entel, J. Hafner, First-principles calculation of the structure and magnetic phases of hematite, *Phys. Rev. B* 69 (2004), 165107.
- [33] S. Grimme, J. Antony, S. Ehrlich, H. Krieg, A consistent and accurate ab initio parametrization of density functional dispersion correction (DFT-D) for the 94 elements H-Pu, *J. Chem. Phys.* 132 (2010), 154104.

[34] Y. Li, Y. Zhao, H. Cheng, Y. Hu, G. Shi, L. Dai, L. Qu, Nitrogen-doped graphene quantum dots with oxygen-rich functional groups, *J. Am. Chem. Soc.* 134 (2012) 15–18.

[35] J. Liu, M. Jiao, L. Lu, H.M. Barkholtz, Y. Li, Y. Wang, L. Jiang, Z. Wu, D.-J. Liu, L. Zhuang, C. Ma, J. Zeng, B. Zhang, D. Su, P. Song, W. Xing, W. Xu, Y. Wang, Z. Jiang, G. Sun, High performance platinum single atom electrocatalyst for oxygen reduction reaction, *Nat. Commun.* 8 (2017) 15938.

[36] J. Liu, Y. Liu, N. Liu, Y. Han, X. Zhang, H. Huang, Y. Lifshitz, S.-T. Lee, J. Zhong, Z. Kang, Metal-free efficient photocatalyst for stable visible water splitting via a two-electron pathway, *Science* 347 (2015) 970–974.

[37] X. Li, W. Bi, L. Zhang, S. Tao, W. Chu, Q. Zhang, Y. Luo, C. Wu, Y. Xie, Single-atom Pt as co-catalyst for enhanced photocatalytic H<sub>2</sub> evolution, *Adv. Mater.* 28 (2016) 2427–2431.

[38] M. Imran, A.B. Yousaf, P. Kasak, A. Zeb, S.J. Zaidi, Highly efficient sustainable photocatalytic Z-scheme hydrogen production from an  $\alpha$ -Fe<sub>2</sub>O<sub>3</sub> engineered ZnCdS heterostructure, *J. Catal.* 353 (2017) 81–88.

[39] K. Zhang, D. Jing, C. Xing, L. Guo, Significantly improved photocatalytic hydrogen production activity over Cd<sub>1-x</sub>NxS photocatalysts prepared by a novel thermal sulfuration method, *Inter. J. Hydrol. Energ.* 32 (2007) 4685–4691.

[40] M. Yu, Z. Wang, J. Liu, F. Sun, P. Yang, J. Qiu, A hierarchically porous and hydrophilic 3D nickel–iron/MXene electrode for accelerating oxygen and hydrogen evolution at high current densities, *Nano Energy* 63 (2019), 103880.

[41] L. Cheng, Q. Chen, J. Li, H. Liu, Boosting the photocatalytic activity of CdLa<sub>2</sub>S<sub>4</sub> for hydrogen production using Ti3C<sub>2</sub> MXene as a co-catalyst, *Appl. Catal. B: Environ.* 267 (2020), 118379.

[42] Y. Cao, G. Wang, Q. Ma, Z. Jin, Amorphous NiCoB nanoalloy modified Mn<sub>0.05</sub>Cd<sub>0.95</sub>S for photocatalytic hydrogen evolution, *Mol. Catal.* 492 (2020), 111001.

[43] X. Liu, Q. Liu, P. Wang, Y. Liu, B. Huang, E.A. Rozhkova, Q. Zhang, Z. Wang, Y. Dai, J. Lu, Efficient photocatalytic H<sub>2</sub> production via rational design of synergistic spatially-separated dual cocatalysts modified Mn<sub>0.5</sub>Cd<sub>0.5</sub>S photocatalyst under visible light irradiation, *Chem. Eng. J.* 337 (2018) 480–487.

[44] S.M. Ji, H. Jun, J.S. Jang, H.C. Son, P.H. Borse, J.S. Lee, Photocatalytic hydrogen production from natural seawater, *J. Photochem. Photobiol. A: Chem.* 189 (2007) 141–144.

[45] W. Li, C. Feng, S. Dai, J. Yue, F. Huo, H. Hou, Fabrication of sulfur-doped g-C<sub>3</sub>N<sub>4</sub>/Au/CdS Z-scheme photocatalyst to improve the photocatalytic performance under visible light, *Appl. Catal. B: Environ.* 168 169 (2015) 465–471.

[46] L. Jia, D.-H. Wang, Y.-X. Huang, A.-W. Xu, H.-Q. Yu, Highly durable N-doped graphene/CdS nanocomposites with enhanced photocatalytic hydrogen evolution from water under visible light irradiation, *J. Phys. Chem. C.* 115 (2011) 11466–11473.

[47] V. Dao, T.T.D. Nguyen, P. Uthirakumar, Y.-H. Cho, G.-C. Kim, J.-K. Yang, D.-T. Tran, T.D. Le, H. Choi, H.Y. Kim, Y.-T. Yu, I.-H. Lee, Insightful understanding of hot-carrier generation and transfer in plasmonic Au@CeO<sub>2</sub> core-shell photocatalysts for light-driven hydrogen evolution improvement, *Appl. Catal. B: Environ.* 286 (2021) 119947.

[48] D. Van Dao, H.D. Jung, T.T.D. Nguyen, S.-W. Ki, H. Son, K.-B. Bae, T.D. Le, Y.-H. Cho, J.-K. Yang, Y.-T. Yu, S. Back, I.-H. Lee, Defect-rich N-doped CeO<sub>2</sub> supported by N-doped graphene as a metal-free plasmonic hydrogen evolution photocatalyst, *J. Mater. Chem. A* 9 (2021) 10217–10230.

[49] S.-W. Cao, X.-F. Liu, Y.-P. Yuan, Z.-Y. Zhang, Y.-S. Liao, J. Fang, S.C.J. Loo, T. C. Sum, C. Xue, Solar-to-fuels conversion over In<sub>2</sub>O<sub>3</sub>/g-C<sub>3</sub>N<sub>4</sub> hybrid photocatalysts, *Appl. Catal. B: Environ.* 147 (2014) 940–946.

[50] M. Imran, A. Bin Yousaf, M. Farooq, P. Kasak, Enhanced Z-scheme visible light photocatalytic hydrogen production over  $\alpha$ -Bi<sub>2</sub>O<sub>3</sub>/CZS heterostructure, *Inter. J. Hydrol. Energ.* 43 (2018) 4256–4264.

[51] A.B. Yousaf, M. Imran, S.J. Zaidi, P. Kasak, Highly efficient photocatalytic Z-scheme hydrogen production over oxygen-deficient WO<sub>3-x</sub> nanorods supported Zn<sub>0.3</sub>Cd<sub>0.7</sub>S heterostructure, *Sci. Rep.* 7 (2017) 6574.

[52] B.-J. Ng, L.K. Putri, L.-L. Tan, P. Pasbakhsh, S.-P. Chai, All-solid-state Z-scheme photocatalyst with carbon nanotubes as an electron mediator for hydrogen evolution under simulated solar light, *Chem. Eng. J.* 316 (2017) 41–49.

[53] X. Wang, G. Liu, Z.-G. Chen, F. Li, L. Wang, G.Q. Lu, H.-M. Cheng, Enhanced photocatalytic hydrogen evolution by prolonging the lifetime of carriers in ZnO/CdS heterostructures, *Chem. Com.* (2009) 3452–3454.

[54] X. Wang, G. Liu, L. Wang, Z.-G. Chen, G.Q. Lu, H.-M. Cheng, ZnO–CdS@Cd heterostructure for effective photocatalytic hydrogen generation, *Adv. Energy Mater.* 2 (2012) 42–46.

[55] D. Van Dao, T.T.D. Nguyen, T.D. Le, S.-H. Kim, J.-K. Yang, I.-H. Lee, Y.-T. Yu, Plasmonically driven photocatalytic hydrogen evolution activity of a Pt-functionalized Au@CeO<sub>2</sub> core-shell catalyst under visible light, *J. Mater. Chem. A* 8 (2020) 7687–7694.

[56] T.P. Trainor, A.M. Chaka, P.J. Eng, M. Newville, G.A. Waychunas, J.G. Catalano, G. E. Brown, Structure and reactivity of the hydrated hematite (0001) surface, *Surf. Sci.* 573 (2004) 204–224.

[57] G. Di Liberto, S. Tosoni, G. Pacchioni, Nature and role of surface junctions in Bi<sub>2</sub>O<sub>3</sub> photocatalysts, *Adv. Funct. Mater.* 31 (2021) 2009472.

[58] G. Di Liberto, S. Tosoni, G. Pacchioni, Z-Scheme versus type-II junction in g-C<sub>3</sub>N<sub>4</sub>/TiO<sub>2</sub> and g-C<sub>3</sub>N<sub>4</sub>/SrTiO<sub>3</sub>/TiO<sub>2</sub> heterostructures, *Catal. Sci. Technol.* 11 (2021) 3589–3598.

[59] J.K. Nørskov, T. Bligaard, A. Logadottir, J.R. Kitchin, J.G. Chen, S. Pandelov, U. Stimming, Trends in the exchange current for hydrogen evolution, *J. Electrochem. Soc.* 152 (2005) J23.

[60] G. Di Liberto, L.A. Cipriano, G. Pacchioni, Universal principles for the rational design of single atom electrocatalysts? Handle with care, *ACS Catal.* 12 (2022) 5846–5856.